



Inverse and 3D forward gravity modelling for the estimation of the crustal thickness of Egypt



Mohamed Sobh^{a,b,*}, Jörg Ebbing^a, Ahmed Hamdi Mansi^{c,d}, Hans-Jürgen Götz^a

^a Institute of Geosciences, Christian-Albrechts-University Kiel, Otto-Hahn-Platz 1, Kiel D-24118, Germany

^b Geodynamics Department, National Research Institute of Astronomy and Geophysics (NRIAG), Helwan, Cairo 11421, Egypt

^c Istituto Nazionale di Geofisica e Vulcanologia, sezione di Pisa, Via U. della Faggiola 32, Pisa 56126 (PI), Italy

^d Department of Civil and Environmental Engineering (DICA), Politecnico di Milano, Piazza Leonardo da Vinci 32, Milano 20133 (MI), Italy

ARTICLE INFO

Keywords:

Gravity inversion
Moho
GOCE
3D density modelling
Egypt

ABSTRACT

A 3D crustal density model for Egypt was compiled. It is constrained by available deep seismic refraction, receiver functions analysis, borehole, and geological data.

In Egypt, seismic data are sparsely and irregularly distributed. Consequently, we developed the crustal thickness model by integrating seismic and gravity data. Satellite gravity data was inverted to build an initial model, which was followed by a detailed 3D forward gravity modelling. The initial crustal thickness is determined by applying seismically constrained non-linear inversion, based on the modified Bott's method and Tikhonov regularization assuming spherical Earth approximation. Moreover, the gravity inversion-based Moho depth estimates are in good agreement with results of seismic studies and are exploited for the 3D forward modelling.

Crustal thicknesses range from 25 to 30 km along the rifted margins of the Red Sea, which thin toward the Mediterranean Sea. Thicknesses in southern Egypt reach values between 35 and 40 km. A maximum crustal thickness of 45 km is found in the southwestern part of Egypt. Within the Sinai Peninsula, the thickness varies from the shallow southern edge (~ 31 km) and increases toward the North (~ 36 km). Our model revealed a thick lower crust beneath the southern part of Egypt, which can be associated with crustal modification that occurred during the collision of East Gondwana and the Saharan Metacraton along the Kerat suture zone during the final assembly of Gondwana in the Neoproterozoic. Finally, the isostatic implications of the differences between the seismic and gravity-derived Mohos are thoroughly discussed.

In conclusion, the developed 3D crustal thickness model provides high-resolution Moho depth estimates that closely resembles the major geological and tectonic features. Also, the existing correlation between the topography, Bouguer anomalies, and Moho depths indicates that the investigated area is close to its isostatic equilibrium.

1. Introduction

The present-day structure and the dynamics of the lithosphere of Egypt and its adjacent regions are controlled by the relative motion of three major tectonic plates: the Eurasia, Africa, and Arabia. The interaction of these continental plate margins causes a complex geodynamic setting. Therefore, mapping the Moho depths can help to understand the crustal structure, the degree and style of the isostatic compensations of continental plates, by lithospheric modelling techniques.

Seismic data, e.g. deep seismic refraction, wide-angle reflection, receiver functions, and ambient noise tomography permit to perform

the most robust imaging of the subsurface, although they are sparsely distributed due to the limited access to the desert of Egypt. Gravity data has better spatial coverage and distribution compared to seismic data and can, therefore, be considered complementary information to resolve the crustal density and thickness variations (Aitken et al., 2013; Ngalamo et al., 2018).

In general, high-resolution mapping of Moho depths is fundamental and results in a better understanding of the geometrical structure of the subsurface and the geodynamical evolution of the study area and, consequently, it can be used for both the prediction and mitigation of geohazards, e.g., earthquakes. Moreover, the knowledge of a precisely

* Corresponding author.

E-mail addresses: mohamed.sobh@ifg.uni-kiel.de (M. Sobh), joerg.ebbing@ifg.uni-kiel.de (J. Ebbing), ahmed.mansi@INGV.it (A.H. Mansi), hajo.goetze@ifg.uni-kiel.de (H.-J. Götz).

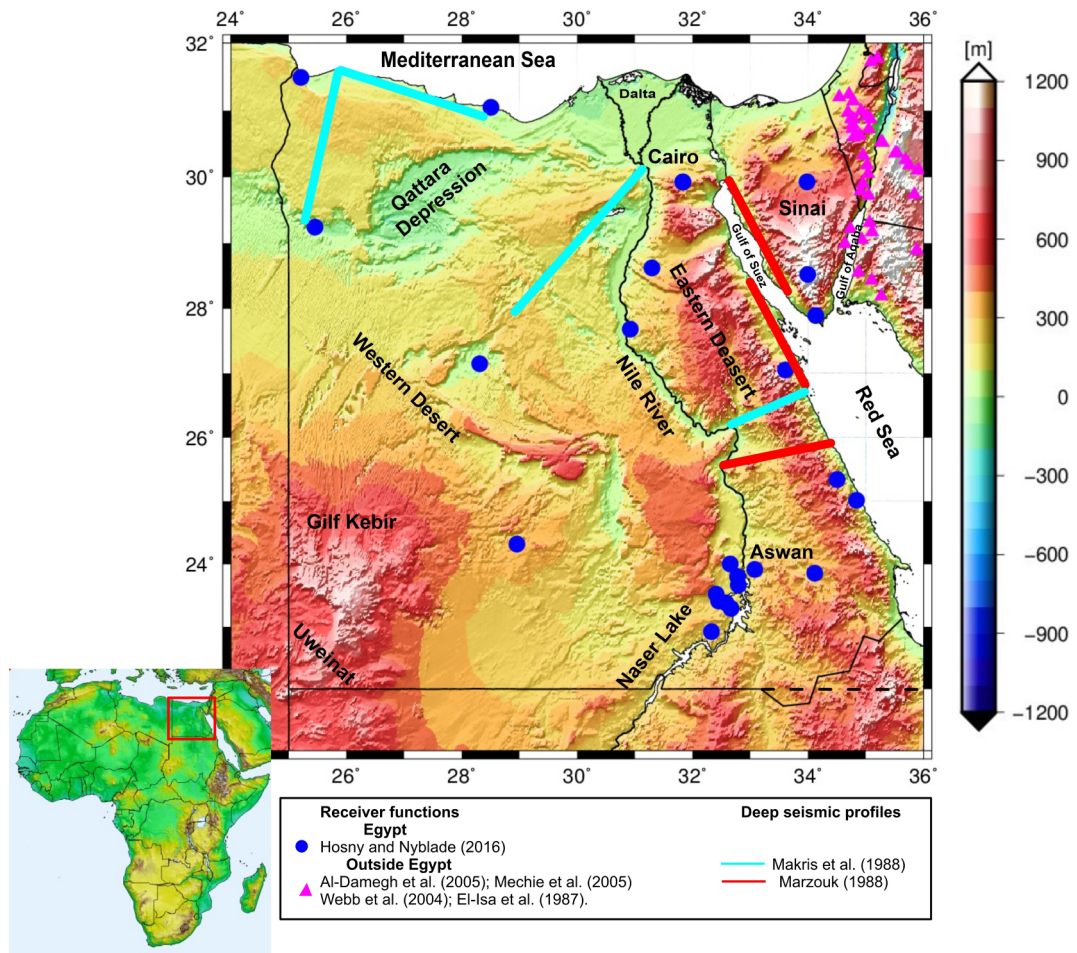


Fig. 1. Geographic map of Egypt and the spatial location of the constraining geophysical data. Cyan lines show the location of deep seismic profiles from Makris et al. (1988). Red lines show the location of the refraction seismic profiles from Marzouk (1988). Blue dots indicate the locations of Egyptian receiver functions (Hosny and Nyblade, 2016) and magenta triangles receiver functions results outside Egypt by El-Isa et al. (1987), Webb et al. (2004), Al-Damegh et al. (2005), and Mechic et al. (2005). The major geographic features are named and positioned correctly. The shaded digital elevation model in the background is derived from the ETOPO1 model (Amante, 2009). (For interpretation of the references to colour in this figure legend, the reader is referred to the web version of this article.)

modelled crust would increase the potential to target and extract natural resources as well as to understand regional dynamics. A better understanding of the deep structures can help to improve the heat flow modelling and the prediction of source rock maturity and hydrocarbon accumulations (Allen and Allen, 2005; Hantschel and Kauerauf, 2009; Bouman et al., 2015).

Regarding Egypt, a number of seismic studies have imaged the crust (Makris et al., 1979; Makris, 1983; Rihm, 1984; Makris et al., 1988; Makris and Rihm, 1991; Rihm et al., 1991; Dorre et al., 1997; Seber et al., 2000; Tealeb et al., 2003; El-Khrepy, 2008; Salah, 2011; Abdelwahed et al., 2013; Hosny and Nyblade, 2014, 2016; Corchete et al., 2017). Most of these studies have explicitly focused on the northern and eastern parts of the study area, i.e. the Red Sea and the Mediterranean Sea coastlines, respectively, while large data gaps away from the coasts exist (Fig. 1).

This study exploits satellite gravity data as well as terrestrial gravity observations acquired over the study area, integrated with the results of the aforementioned major seismic experiments as physical constraints for the development of the crustal thickness model as well as to perform an interdisciplinary interpretation.

Since seismic data in Egypt are sparse and irregularly distributed, the main objective of this study is to develop a crustal thickness model for Egypt (Fig. 1) by integrating both seismic and gravity data. First,

satellite gravity data is inverted in order to build an initial crustal thickness map precedent to performing a detailed 3D forward gravity model constrained by independent information. Because the variations in the Moho boundary depth correspond to different geological terranes, we compare the Moho map with the major surface geological units within the study area.

This paper commences with a summary of Egyptian geological and tectonic settings in Section 2. The data exploited for the present and previous Moho depths estimates are thoroughly presented in Section 3. The implemented theory and methodology for the development of the gravity-based Moho model, assessment of the isostatic state of the study area, and the application of the necessary corrections as well as the gravity inversion, and the compilation of the 3D forward gravity modelling are described in Section 4. The analyses and the final Moho depths model are presented in Section 5. The discussion is held in Section 6, while relevant conclusions are drawn in Section 7.

2. Tectonic settings and former geophysical studies

This section is dedicated to the description of the tectonic settings and the inspection of the previous Moho depths estimations carried out in the study area.

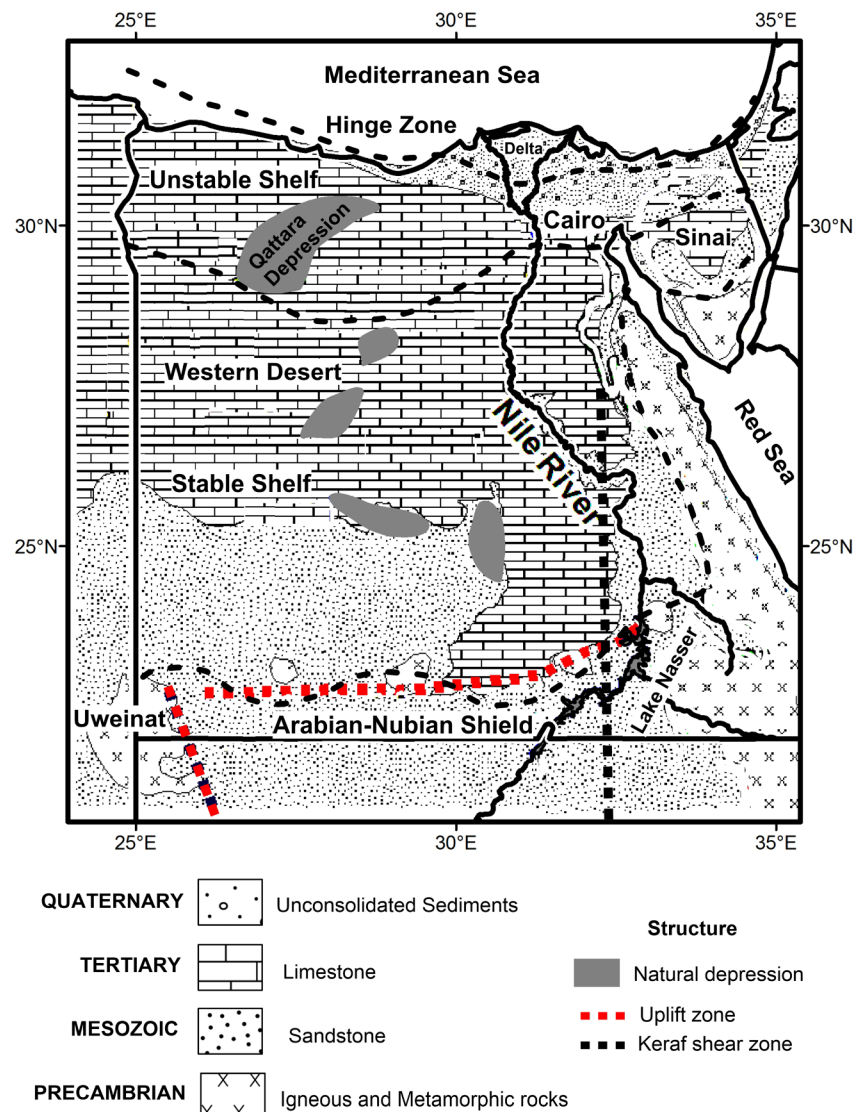


Fig. 2. A simplified geologic map of Egypt, redrawn after the geological map from 1981 of the Egyptian Geological Survey and Mining Authority (1981). Black dashed lines show boundaries of the main tectonic provinces (Said, 1962), which are of particular interest for interpretation of modelling and inversion results.

2.1. Tectonic and geological settings of Egypt

Egypt is primarily divided into four major provinces; the Arabian-Nubian Shield, stable shelf, unstable shelf, and the Gulf of Suez-Red Sea graben (Said, 1962). The Arabian-Nubian Shield that mainly consists of Precambrian rocks, extends over large parts of the Eastern Desert, the southern Sinai Peninsula, and the extreme southern part of the Western Desert at the Uweinat area (southwest of Egypt). The stable shelf, located in the North and the West of the Arabian-Nubian Shield, exhibits gentle tectonic deformations, where the continental and epicontinental deposits, e.g. the Mesozoic Nubian Sandstone mainly represent its sedimentary cover. The sedimentary sequence on the stable shelf is relatively thin of about 400 m near the Arabian-Nubian Shield and increases to, as thicker as, 2500 m near the transition zone into the unstable shelf in the North. The Hinge Zone, located between the mobile shelf and the miogeosynclinal basinal area, is characterized by a rapid thickening of the Oligocene to Pliocene sediments and partially coincides with the present Mediterranean coastal area (Fig. 2).

However, in southern Egypt, a number of granitic outcrops have been interpreted to be part of the much older Saharan Metacraton. Fig. 2 displays a simplified geologic map of Egypt and its main tectonic provinces. The suture between the Neoproterozoic terranes to the East

and the Metacraton to the West is marked by the Keraf shear zone (Abdelsalam and Stern, 1996a; Abdelsalam et al., 1998). On the one side, the Phanerozoic sedimentary rocks overlie the Precambrian basement across the majority of the Egyptian territory. On the other side, the Palaeozoic sandstones and shales are found at the base of the sedimentary section, which in many places are overlain by the Mesozoic sandstones, Paleogene and Neogene limestones, sandstones, and conglomerates, and unconsolidated Quaternary sediments (Abdelsalam and Stern, 1996b; Abdelsalam et al., 1998).

2.2. Previous Moho depths studies of Egypt

The crustal thickness of Egypt has been previously investigated in a number of studies, summarised in Table 1 and Fig. 1. However, most of these studies focused on the northern and eastern parts of the country, along the Red Sea and the Mediterranean Sea, respectively, by elaborating the older seismic refraction, receiver functions studies, and terrestrial/ground gravity measurements. Specifically, most of such studies are based on seismological analyses, e.g., local earthquake travel time inversion (Abdelwahed et al., 2013), seismic profiles (Makris et al., 1979; Makris, 1983; Gaulier et al., 1988; Marzouk, 1988; Makris and Rihm, 1991; Rihm et al., 1991), and deep seismic sounding (Ginzburg

Table 1

Moho depths of previous investigations for Egypt (see Fig. 1). The methodology used is also given; units in [km].

Area	References	Method	Depth estimates
Sinai Peninsula	Marzouk (1988) Saleh et al. (2006) Abdelwahed et al. (2013) Ginzburg et al. (1981) Hosny and Nyblade (2016) Corchete et al. (2017)	Seismic refraction Gravity Local earthquake travel time inversion Deep Seismic Sounding Receiver Functions Rayleigh wave analysis	30–35 31 31–35 33–35 32–38 30–35
Northern Egypt and South-East Mediterranean	Makris et al. (1991) Segev et al. (2006) Dorre et al. (1997) Abdelwahed et al. (2013) Salah (2011) El-Khrepy (2001)	Seismic refraction Deep Seismic Sounding Gravity Local earthquake travel time inversion Receiver Functions Seismic refraction	30–32 30–35 30–32 29–31 31 33
NW Red-Sea	Makris et al. (1979)	Seismic refraction	32.5
Cairo	Makris et al. (1979)	Seismic refraction	31–33
Fayoum	Marzouk (1988)	Seismic refraction	32
Dahshour	Dorre et al. (1997)	Gravity	30–32
Middle Egypt	Abdelwahed et al. (2013) EL-Hadidy (1995)	Local earthquake travel time inversion Deep Seismic Sounding	32–33 31
Western Desert	Makris et al. (1988) Dorre et al. (1997) Abdelwahed et al. (2013)	Seismic refraction Gravity Local earthquake travel time inversion	33–35 32–34 38
Upper Egypt	Makris et al. (1988) Dorre et al. (1997) Abdelwahed et al. (2013) Hosny and Nyblade (2016)	Seismic refraction Gravity Local earthquake travel time inversion Receiver Functions	34 32–34 35–40 35–40
Eastern Desert	Makris et al. (1991)	Seismic refraction	30–35
Northern Red Sea	Rihm et al. (1991) Saleh et al. (2006) Abdelwahed et al. (2013)	Seismic refraction Gravity Local earthquake travel time inversion	30–32 31 29–31

et al., 1981; EL-Hadidy, 1995; Segev et al., 2006). Corcete et al. (2017) determined the crustal and uppermost mantle structure in the north-eastern Egypt based on the Rayleigh wave analyses. While, Hosny and Nyblade (2014) modelled the P-wave receiver functions around Lake Nasser in southern Egypt, for a single station in north-eastern Egypt and they extended their research to include the all-broadband beneath all seismic stations in Egypt (Hosny and Nyblade, 2016).

In addition to the aforementioned seismic investigations, a number of gravity-based calculations of the crustal thickness have been reported. Dorre et al. (1997) compiled a crustal thickness variation map for Egypt by the use of 2.5D gravity models. They used the gravity data collected within the framework of the African Gravity Project (Fairhead et al., 1988), which encompasses both the terrestrial and airborne measurements and applied the 2D power spectrum analysis.

Seber et al. (2000) estimated the crustal thickness of the Middle East, in general, and Egypt, in particular, integrating gravity data with refraction seismic profiles. Moreover, **Saleh (2012)** reported the Moho depths along the Nile Delta utilising the 3D forward gravity and magnetic modelling constrained by the available seismic reflection and well logs data. After this brief overview of the past Moho-related studies, the next section will describe the new gravity datasets exploited, in our investigations, to determine a country-wide Moho depths, which is a combination of the terrestrial and satellite gravity measurements.

3. Database

This section is concerned with the description of the various gravity datasets used in this study as well as the procedure followed for the data correction.

3.1. Gravity data

Two different gravity field datasets were exploited: (1) the Gravity Field and Steady-State Ocean Circulation Explorer (GOCE)-based dataset, which was utilised to build the initial Moho depth estimation via the gravity inversion and (2) a high-resolution combined (terrestrial

and satellite gravity) dataset that was used to build the detailed 3D density model.

3.1.1. High resolution gravity data

A new combined regional gravity model has been developed for Egypt integrating the recently-made-available terrestrial free-air (FA) gravity anomalies with satellite-based gravity observations (Sobh et al., 2018). The terrestrial data used in this study, characterized with consistent gravity and height values, are exploited for the first time over the Egyptian territory.

3.1.2. Gravity data processing

With regard to the data processing, one has to consider that the gravity observations at the Earth's surface and the Earth near space vary from the theoretical "normal" gravity field values. The signal magnitude is not caused only by the latitude effect but also the elevation of observational points, the density of the cap beneath the station in the subsurface, and the effect of the topographic/bathymetric masses in the vicinity/surrounding. After correcting the gravity measurements for the Earth tidal effects and the air pressure variations, the remaining time-invariable residuals of the observed signal are theoretically: the normal gravity (γ_0), the effect of topographic/bathymetric masses (δg_{TC}), the Bouguer slab (δg_{BPL}), the elevation effect (synonym to the FA term) (δg_{FA}), and the effect of the crustal root (δg_R).

The common representations of the gravity measurements, as maps and profiles, depend on the applied corrections to the gravity measurements. From all the measured values, the normal gravity value is always subtracted and therefore the term “gravity anomaly” is defined. This is simply the difference between the observed and the “normal” gravity values.

In geophysics, the main three anomalies, i.e. the FA anomaly, Bouguer anomaly (BA), and isostatic anomaly (ISA), are distinguished in order to define the gravity field in terms of the height of the observations (e.g., Naudy and Neumann, 1965; LaFehr, 1991; Li and Götze, 2001; Hackney and Featherstone, 2003; and many others).

Using the δg_R , which accounts for the effects of a mountain root, one

can easily define the FA, BA, and ISA as follow:

$$FA = \Delta g'_o = \delta g_{obs} + \delta g_{FA} + g_{TC} - \gamma_0 \quad (1)$$

$$BA = \Delta g''_o = \delta g_{obs} + \delta g_{FA} + \delta g_{TC} + \delta g_{BPL} - \gamma_0 \quad (2)$$

$$ISA = \Delta g_{ISA} = \delta g_{obs} + \delta g_{FA} + \delta g_{TC} + \delta g_{BPL} + \delta g_R - \gamma_0 \quad (3)$$

Based on the objective of the survey, specific corrections must be considered, in order to process the observations, g_{obs} . The calculation of the topographic reduction (δg_{TOP}) necessitates the precise knowledge of the topography/bathymetry, which is commonly given in terms of a digital elevation model (DEM), and the surface densities, is normally performed using an area of influence, e.g., a surrounding circular area of 50–167 km radius (LaFehr, 1991; Hinze et al., 2005). However, Mikuška et al. (2006) studied the so-called “long distant relief effects” and recommended the calculation of the effects of all the topographic masses on Earth. The gravity effects of a Bouguer slab with a certain thickness value, which is defined by the difference between the physical station height and a reference level, which is normally taken as the geoid, should always be calculated as a spherical cap (Baschlin, 1948). For smaller areas (with an influence radius $R < 20$ km) and moderate terrain roughness, the Bouguer slab can be simply calculated by:

$$\Delta g_{BPL} = 2\pi G\rho(H_S - H_B) \quad (4)$$

where G is the gravitational constant ($6.672 \cdot 10^{-11} \text{ m}^3 \cdot \text{s}^{-2} \cdot \text{kg}^{-1}$), ρ is the crustal density ($2670 \text{ kg} \cdot \text{m}^{-3}$), H_S is the topographic height or the bathymetric depth of the gravity station, and H_B is the reference height (usually it refers to the geoid).

In the last step, the FA effects, δg_{FA} , is calculated using the “normal gradient” relationship, where (the vertical gravity gradient is 0.3086 mGal/m , where $1 \text{ mGal} = 1 \times 10^{-5} \text{ m} \cdot \text{s}^{-2}$): $g_{FA} = 0.3086 \cdot (H_S - H_B) \text{ mGal/m}$.

It is worth mentioning that the implementation of a constant gravity gradient is limited to large-scale investigations and it has to be replaced by equivalent values of the derivation of closed-mathematical expressions of the normal gravity, which is always both latitude and height dependent.

The BA field is nothing but correcting the FA gravity anomaly signal for the topography correction (TC) before being used within the modelling step, as follows:

$$BA = FA - TC \quad (5)$$

The TC signal has been computed, using the gravity terrain effects (GTE) package (Sampietro et al., 2016; Capponi et al., 2018) with a continental crustal density of $2670 \text{ kg} \cdot \text{m}^{-3}$ and $1630 \text{ kg} \cdot \text{m}^{-3}$ for the offshore. For each station, the gravitational effect of the prisms inside a circle with radius (167 km) around the station is computed, where all the first and second spherical corrections of the Earth's shape (Braitenberg et al., 2016; Mansi, 2016) have been considered.

The FA values of the study area, shown in Fig. 3 a, range between -45 and 110 mGal and they are found to be strongly correlated with the topography. The Arabian-Nubian Shield, which is a stable tectonic unit that consists of the exposed basement rocks in the Eastern Desert, the southern part of the Sinai Peninsula and the isolated outcrops in southern Egypt, is characterized with positive FA anomalies. The north-western part of Egypt is characterized with a positive FA anomaly (up to 70 mGal), whose value decreases toward the Mediterranean coast ($\sim 45 \text{ mGal}$). The Nile Delta is characterized with a negative FA anomaly ($\sim -27 \text{ mGal}$) that increases toward the Mediterranean coastline ($\sim 30 \text{ mGal}$). On the meanwhile, the FA gravity anomalies along the Nile River have negative values ($\sim -15 \text{ mGal}$). A series of elongated high-value gravity signal parallel to the overall Red Sea trend is located outside the axial rift.

The computed TC signal varies between -10 and 120 mGal (Fig. 3

b), which naturally shows a strong correlation with the topography as it solely depends on the elevation. The Uweinat area, the locality of high mountains, has the highest TC value ($\sim 120 \text{ mGal}$), where the Qattara Depression, where the lowest altitude values are found, has a negative TC value ($\sim -2 \text{ mGal}$). The BA, shown in Fig. 3 c, was obtained subtracting the TC values from the FA gravity signal.

The errors of the BA signal has been estimated propagating the uncertainties of both the observed gravity measurements and the computed TC signal. The exploited high-resolution gravity dataset consists of a total number of 56,250 ground stations integrated with satellite-based gravity data via the classical remove-compute-restore technique and the collocation procedure. The data provider has suggested an accuracy of 1.0 mGal for such terrestrial data. However, it is expected that the accuracy of the provided FA gravity anomalies, due to the noticeable high-inhomogeneity should be substantially low ($\sim 5 \text{ mGal}$) over the majority of the study area (Sobh et al., 2018).

The TC signal has an error of about 2.0 mGal , which comes from the mean error of the Shuttle Radar Topography Mission (SRTM) equivalent to 6.0 m , as reported by Rodriguez et al. (2006). A note must be taken that the computed TC signal assumed a constant density for all rock masses above the mean sea level, which might introduce additional errors.

In general, the continental part of the study area is characterized by negative BA values, whereas the northern part, along the coastal area of the Mediterranean Sea, is characterized by positive values ($> 50 \text{ mGal}$). In the meanwhile, the Nile Delta is characterized by pronounced negative BA values in the East-West direction (-35 mGal), whereas the northern delta has positive anomalies ($> 50 \text{ mGal}$) that occupy the coastal area of the Mediterranean Sea. The southwestern part of Egypt has a negative BA footprint that coincides with the Uweinat area.

The highest mountains, located at the shoreline of the Red Sea (altitudes greater than 1000 m), are characterized by negative BA values that range between -30 and -10 mGal . These BA values reveal that the crust attains its maximum thickness below the Red Sea Mountains and considerably thins toward the Red Sea Rift (Saleh et al., 2006).

3.1.3. GOCE satellite data

The Gravity Observation COmbination fifth release (GOCO05) model (Mayer-Guerr, 2015) is used to synthesize the BA signal at a constant altitude, in this study, at 50 km above the ellipsoid. The GOCO05 model is developed up to a spherical harmonic degree/order 280 and was built using the full GOCE mission data with a spatial resolution of about 70 km . The synthesized BA signal is then inverted in order to obtain the initial estimates of the Moho depths.

The TC for the GOCE-based data was computed using the Tesseroids (Uieda et al., 2016) using the 1 arc-min spatial resolution ETOPO1 model (Amante, 2009). A continental crustal density of $2670 \text{ kg} \cdot \text{m}^{-3}$ and $1630 \text{ kg} \cdot \text{m}^{-3}$ for the offshore were applied. A 5-degree padding has been used in all directions, extending the actual DEM, i.e. topography/bathymetry, of the study area to avoid any edge effects even for the far-field topography (Szwilus et al., 2016; Mansi et al., 2018; Sampietro et al., 2018a; Sampietro et al., 2018b; Zaki et al., 2018a; Zaki et al., 2018b). The BA signal calculated from GOCE data is reported in Fig. 3 d.

3.2. Constraining data for the 3D modelling procedure

The initial model consists of four layers, namely, the sediments, two different crustal domains, and the upper mantle. Moreover, the initial model takes all the significant geological and geophysical observations into the consideration. Subsequently, the free parameters of the initial model can be modified until the forward computed gravity signal best-fit the measured values.

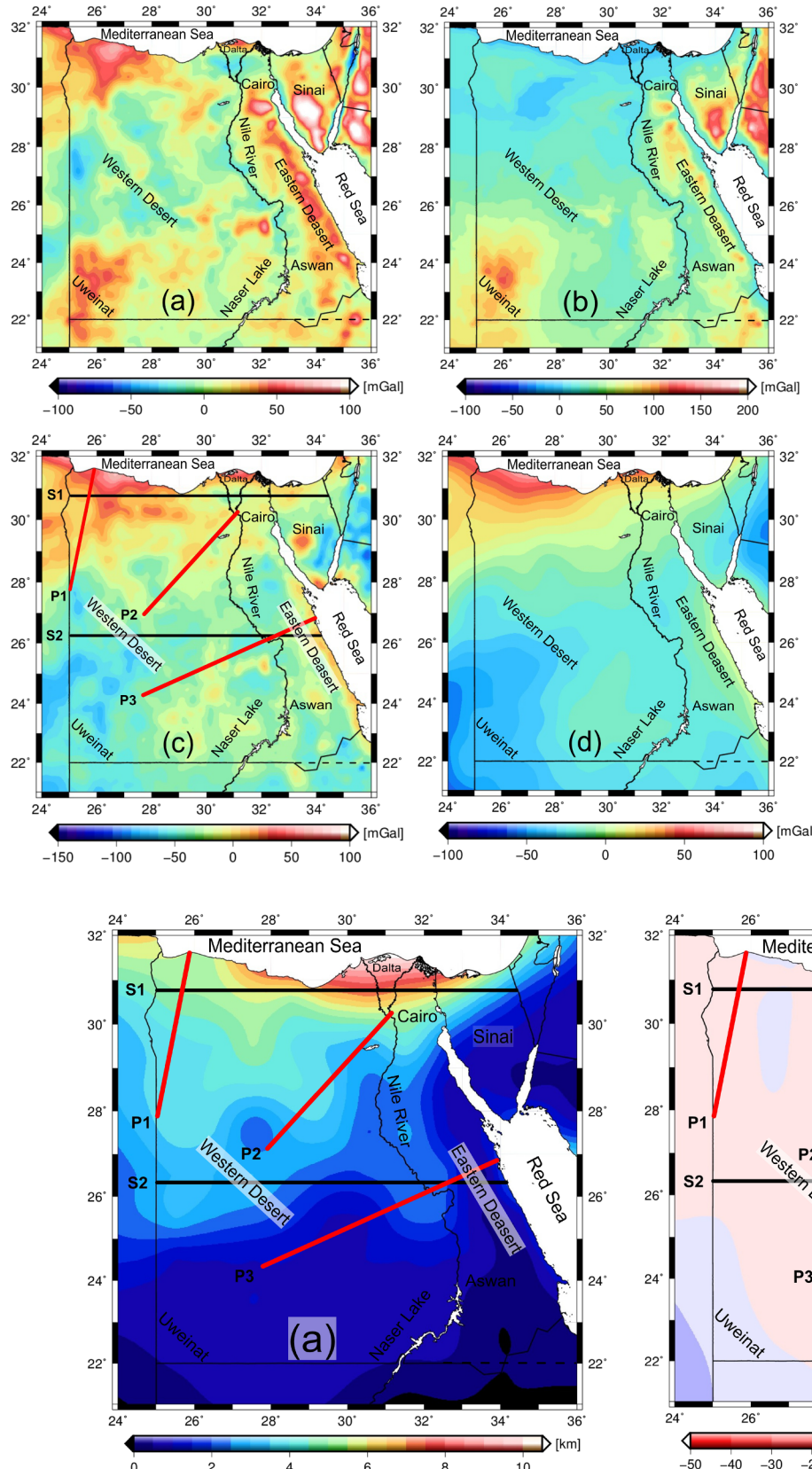


Fig. 3. The compilation of gravity and topographic maps. (a) The Free-air anomaly from the combined regional gravity model (Sobh et al., 2018), (b) the topographic correction computed using the GTE software (Sampietro et al., 2016; Capponi et al., 2018), (c) the Bouguer gravity anomaly obtained by subtracting the field in (b) from the field in (a), and (d) shows the Bouguer gravity of the GOCE-based satellite signal in panel (d) has been inverted for the Moho surface estimation. The three solid red lines show the locations of three constraining seismic refraction profiles. Black lines indicate the locations of the density forward model cross-sections S1 and S2. Units in [mGal]. (For interpretation of the references to colour in this figure legend, the reader is referred to the web version of this article.)

Fig. 4. The two types of model constraints. (a) Sediment thickness from Exxon 1985; units given in [km]. (b) Upper mantle density configuration at 50 km depth, converted from the SL2103Sv model (Schaeffer and Lebedev, 2013); units in [$\text{km} \cdot \text{m}^{-3}$]. The major geographic features are named and geographically positioned. Red solid lines show the locations of the three seismic refraction profiles P1–P3 (refer to text). Black lines show the locations of the density forward model cross-sections S1 and S2. (For interpretation of the references to colour in this figure legend, the reader is referred to the web version of this article.)

Table 2

The density values used for the 3D forward modelling; units in [km·m⁻³].

Layer	Density	Reference
Sediments	2400	Ginzburg and Ben-Avraham (1987), Makris et al. (1994)
Upper crust	2700	Abdelrahman et al. (1988), Ginzburg and Ben-Avraham (1987), Makris et al. (1994)
Lower crust	2900	Ginzburg and Ben-Avraham (1987), Jacobs et al. (1959), Makris et al. (1979, 1994), Prodehl and Mechle (1991), Rihm et al. (1991)
Upper mantle	3250–3300	Ginzburg and Ben-Avraham (1987), Jacobs et al. (1959), Makris et al. (1994)

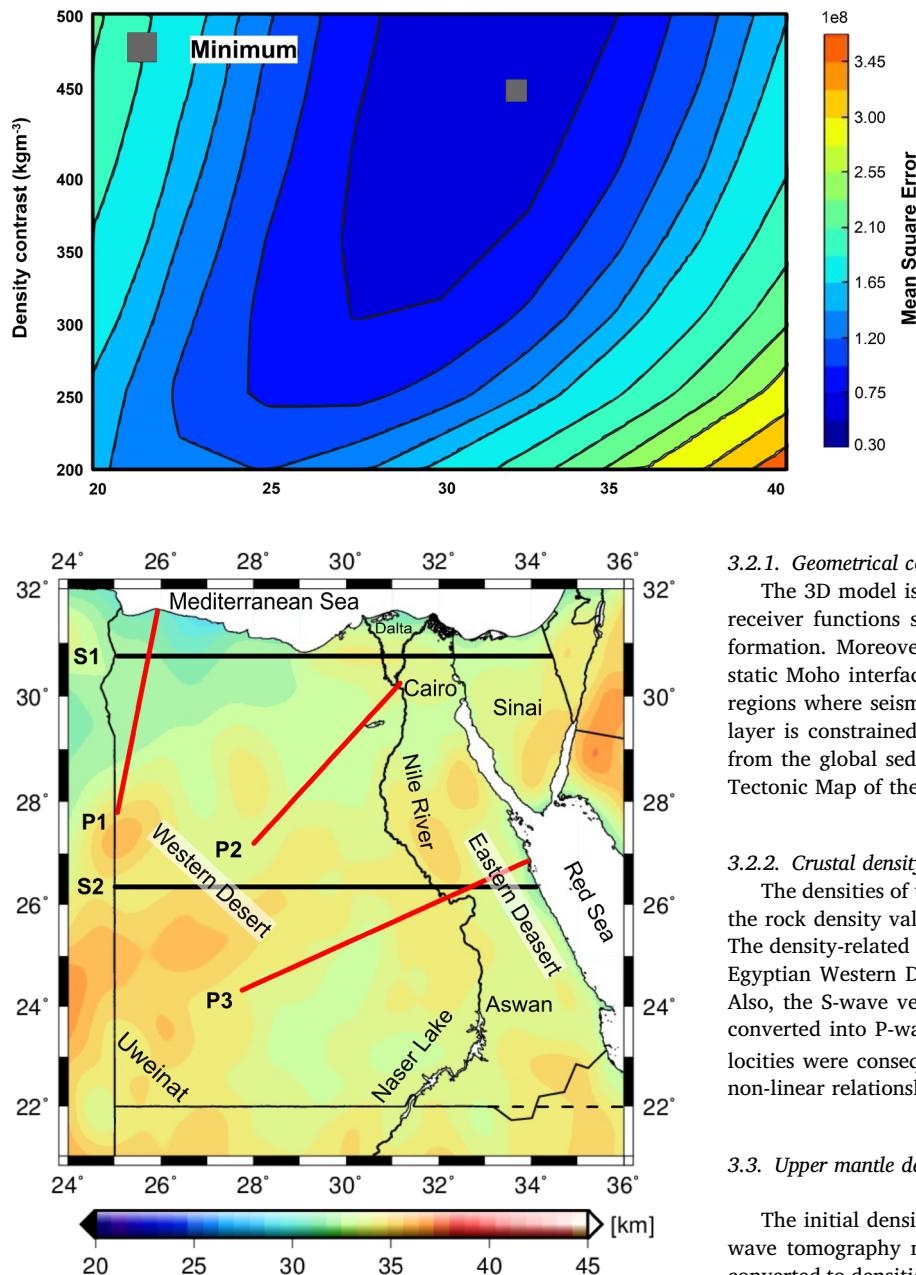


Fig. 5. The validation step exploited to determine the Moho reference level (Z_{ref}) and the density contrast ($\Delta\rho$). The colours represent the Mean Square Error. The best-fit model is marked by the grey rectangular, which indicates a density contrast of $450 \text{ km}\cdot\text{m}^{-3}$ and a Moho reference depth of 32 km. (For interpretation of the references to colour in this figure legend, the reader is referred to the web version of this article.)

Fig. 5. The validation step exploited to determine the Moho reference level (Z_{ref}) and the density contrast ($\Delta\rho$). The colours represent the Mean Square Error. The best-fit model is marked by the grey rectangular, which indicates a density contrast of $450 \text{ km}\cdot\text{m}^{-3}$ and a Moho reference depth of 32 km. (For interpretation of the references to colour in this figure legend, the reader is referred to the web version of this article.)

3.2.1. Geometrical constraints

The 3D model is initially constrained by the deep seismic profiles, receiver functions studies (Fig. 1), borehole logs, and geological information. Moreover, the gravity inversion-based Moho and the isostatic Moho interface are used to constrain the Moho depths in these regions where seismic observations are null. Besides, the sedimentary layer is constrained by the thickness data of the sediments retrieved from the global sediment thickness (Fig. 4) compilation of the Exxon Tectonic Map of the World (Exxon, 1985).

3.2.2. Crustal density constraints

The densities of the crustal models of Egypt were defined exploiting the rock density values of the various studies, summarised in Table 2. The density-related studies were carried out in the northern part of the Egyptian Western Desert, the Nile Delta, and the Mediterranean Sea. Also, the S-wave vertical profiles of Hosny and Nyblade (2016) were converted into P-wave velocities using the $\frac{v_p}{v_s}$ ratio. These P-wave velocities were consequently transformed into densities by applying the non-linear relationships of Christensen and Mooney (1995).

3.3. Upper mantle density constraints

The initial density of the upper mantle is obtained based on the S-wave tomography model of Schaeffer and Lebedev (2013), which is converted to densities in two steps: first, the P-wave velocities (v_p) were calculated from the S-wave velocity (v_s), then in turn the obtained P-wave velocities were converted into densities (Kaban et al., 2016). The upper mantle density structure at 50 km depths is shown in Fig. 4 b. The model demonstrates very small density changes.

Accordingly, the density of the lithospheric upper mantle was assumed to be laterally homogeneous with a density value of $3300 \text{ km}\cdot\text{m}^{-3}$ as the main focus of this study is on the crustal structure itself with the exception toward the Red Sea in the West-East direction.

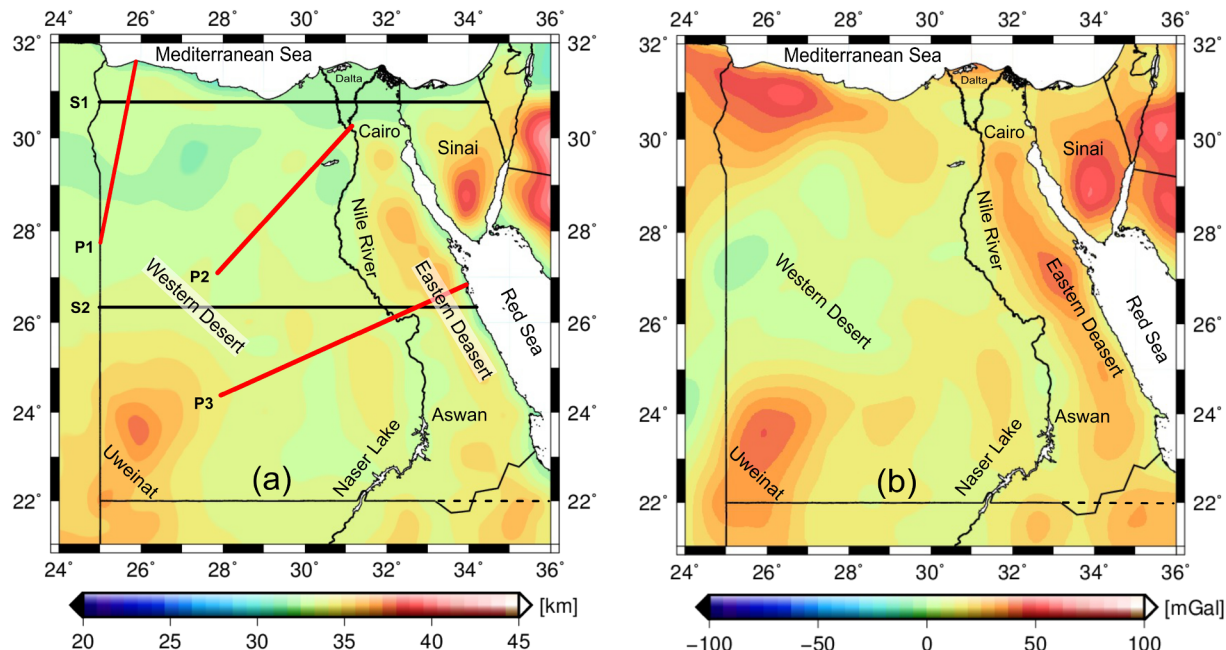


Fig. 7. (a) The Airy-isostatic Moho depth estimates assume a density contrast of $450 \text{ km} \cdot \text{m}^{-3}$ of the crust-mantle interface and a reference depth of 32 km; units given in [km]. (b) The isostatic gravity residual field; units in [mGal]. The major geographic features are named and geographically positioned. Red solid lines show the locations of the three seismic refraction profiles (refer to previous figures). Black lines show the locations of the density model cross-sections S1 and S2. (For interpretation of the references to colour in this figure legend, the reader is referred to the web version of this article.)

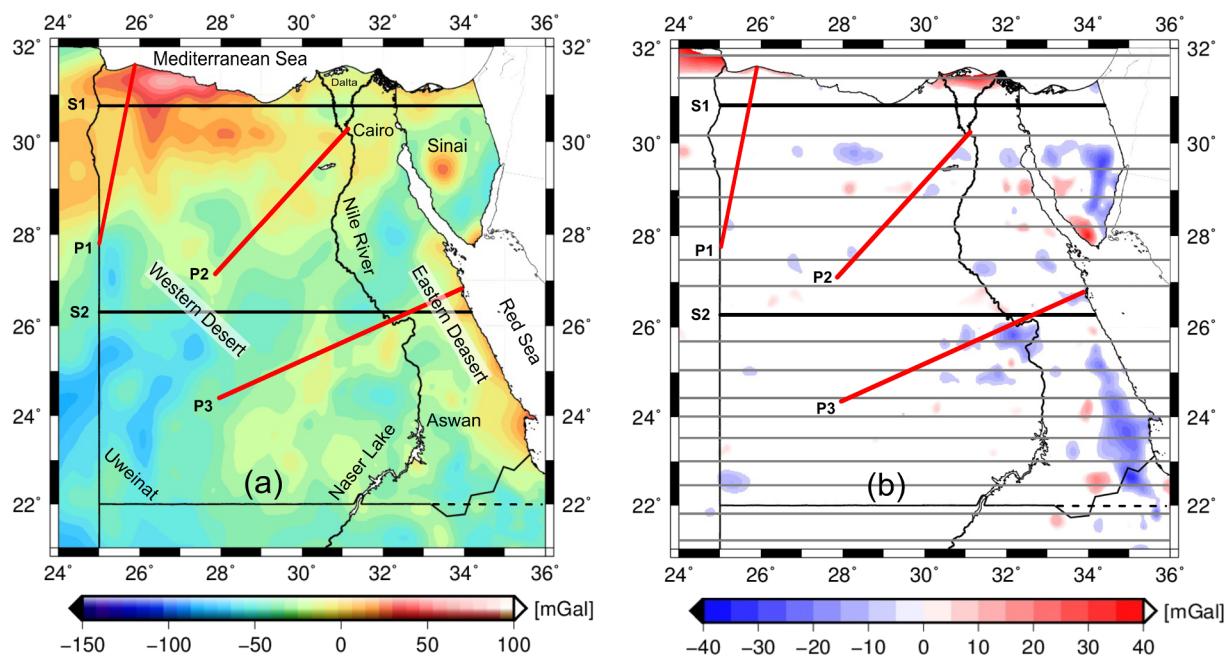


Fig. 8. The comparison of the calculated and modelled Bouguer gravity fields. (a) The calculated Bouguer gravity map for Egypt and (b) the gravity residuals, which result from subtraction of the Bouguer gravity field (a) and the 3D modelled gravity. Grey lines show the location of the IGMAS+ modelling vertical sections. The major geographic features are named and geographically positioned. Red solid lines show the locations of the three seismic refraction profiles (refer to previous figures). Black lines show the locations of the density model cross-sections S1 and S2; units in [mGal]. (For interpretation of the references to colour in this figure legend, the reader is referred to the web version of this article.)

4. Methods

The space-wise approach (Sampietro et al., 2017) has been applied for the data integration then the 3D density modelling, which incorporates forward and inversion techniques, was performed, where the geometry for the structural and the density model have been defined.

4.1. Gravity inversion

In order to get preliminary information about the crustal thicknesses of Egypt, a regularized non-linear gravity inversion was applied (Uieda and Barbosa, 2017). The method is based on the modified Bott's method (Silva et al., 2014) with the Tikhonov regularization to stabilize the

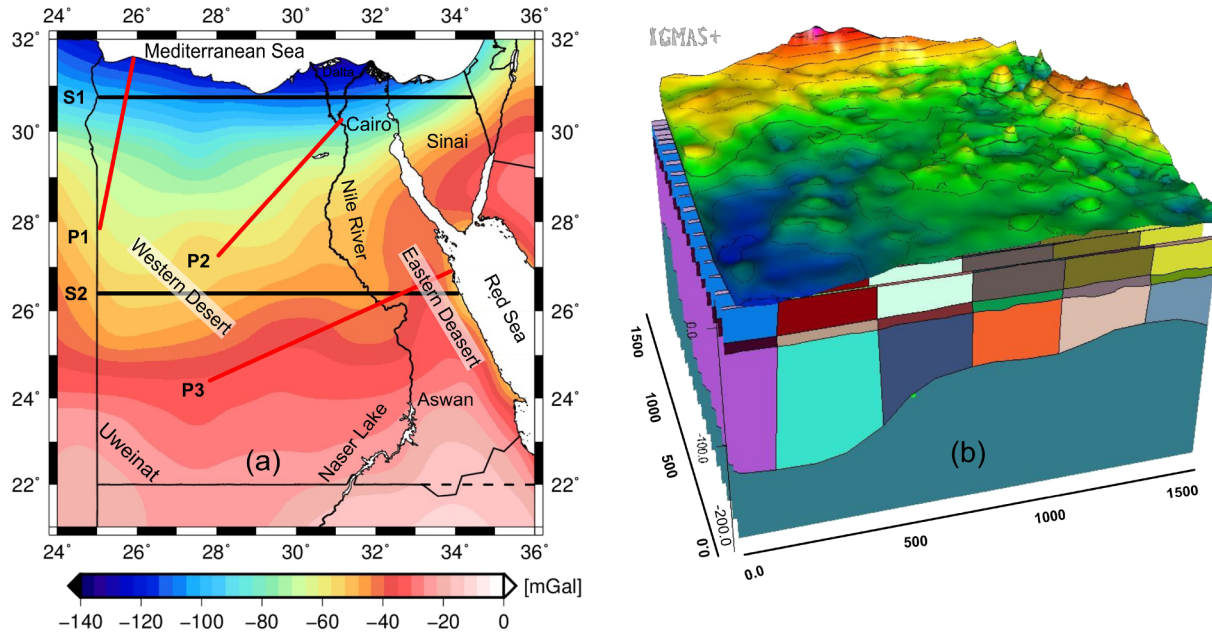


Fig. 9. Modelling results. (a) The gravity effects of the sediments. The gravity increases with the sediment thickness; units in [mGal]. (b) The three-dimensional perspective view of the IGMAS+ density model with the Bouguer gravity anomaly placed on top. The major geographic features are named and geographically positioned. Red solid lines show the locations of the three seismic refraction profiles (refer to previous figures). Black lines show the locations of the density model cross-sections S1 and S2. (For interpretation of the references to colour in this figure legend, the reader is referred to the web version of this article.)

computed solutions in a two-step procedure. In the first step, the regularization parameters are determined using a predefined set of initial values for the mean depth and the density contrast of the Moho discontinuity. In the second step, the gravimetric inversion is carried out for a set of different mean depth and density contrast values, where the best estimate, i.e. the final solution, is obtained after the cross-comparison with the seismic-based Moho depth estimates is held.

For such a purpose, the GOCE-synthesized BA signal at an ellipsoidal height of 50 km is inverted. The results of the gravity inversion are controlled by two parameters namely, the Moho reference depth and the density contrast between the crust and the upper mantle. Therefore, the available seismic data displayed in Fig. 1, were used to validate the obtained results by examining all the possible combinations of the nine Moho reference depth values that range from 20 to 40 km with a 2.5 km incremental step, and the seven density contrast values that range between 200 and 500 $\text{km} \cdot \text{m}^{-3}$ with 50 $\text{km} \cdot \text{m}^{-3}$ intervals. Fig. 5 visualises the Mean Square Error (MSE) values with respect to the seismological Moho dataset. The optimal MSE value has been obtained using the 32 km reference Moho depth and the 450 $\text{km} \cdot \text{m}^{-3}$ density contrast. The gravity residuals appear to follow a Gaussian distribution with a mean value of 0.23 mGal and a standard deviation (STD) of 2.56 mGal. The obtained Moho depths model varies between 20 and 40 km as shown in Fig. 6.

4.2. 3D Modelling with IGMAS+

In order to compile a 3D model for Egypt, the Interactive Geophysical Modelling Assistant (IGMAS+) software has been used, which is a 3D geo-modelling package developed based on the simultaneous forward modelling of gravity, gravity gradients, and magnetic fields (Götze and Lahmeyer, 1988; Schmidt et al., 2010; Alvers et al., 2014; Alvers et al., 2015; Schmidt et al., 2015). The IGMAS+ platform offers an interdisciplinary 3D modelling approach integrating independent seismic, boreholes, and geological datasets, thusly reducing the ambiguity of the potential field inversion. The model consists of several parallel cross-sections, in which the vertical sections run from

the East to the West direction with a separation offset of 50 to 100 km. The implemented IGMAS+ algorithm automatically eliminates the edge effects of a limited 3D model.

4.3. Isostasy modelling

In order to calculate the isostatic state of the lithosphere in Egypt, the Airy-isostatic correction is applied to the BA values, which, therefore, removes a significant part of the effects of the dominating deep density heterogeneity of the BA signal. Such a correction assumes that the crust is compensated by variations of the Moho depths. First, the root effects are computed and later removed from the BA signal to obtain the residual isostatic gravity field. The Airy-isostatic Moho (Eq. (6)) is then calculated using the topography/bathymetry data provided by the ETOPO1 model (Amante, 2009).

For comparison purposes, a reference Moho depth value has to be used, which can be reasonably retrieved from the previous Moho depth studies carried out in the study area. Abdelwahed et al. (2013) and Hosny and Nyblade (2016) estimated the Moho depths, displayed in Fig. 7 a, which range between 30 and 35 km in most parts of Egypt. Consequently, the reference Moho depth is set to 32 km.

$$M_{iso} = Moho_{ref} + \frac{\rho_m}{\rho_m - \rho_c} * A_{topo} \quad (6)$$

where ρ_c and ρ_m are the crust and mantle density, respectively, the $Moho_{ref}$ is the Moho reference depth, and A_{topo} is the equivalent topography, which is calculated to account for the areas below the sea level:

$$A_{topo} = k * t \quad (7)$$

where $k = 1 \text{ km} \cdot \text{m}^{-3}$ for the onshore regions and $k = \frac{2670 - 1030}{2670} \text{ km} \cdot \text{m}^{-3}$ for the offshore area.

On the other hand, the reference Moho density contrast value is set equivalent to 450 $\text{km} \cdot \text{m}^{-3}$, a value of which generally corresponds to the petrological data (Rabbel et al., 2013).

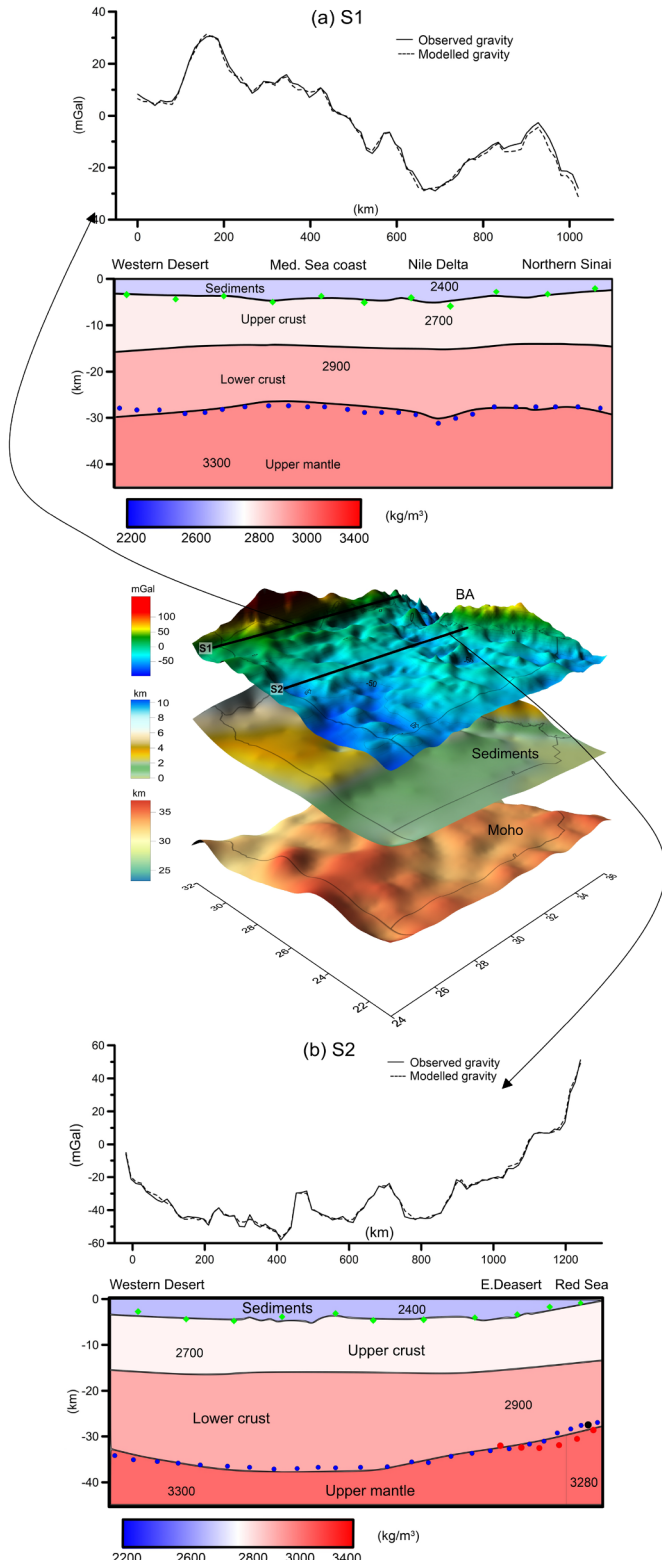


Fig. 10. Details of the modelling results along the seismic profiles S1 in (a) and S2 in (b). The perspective views of the 3D Moho interface, the modelled sediment interfaces, and the Bouguer anomaly of the area are shown in between the profiles in the center of the Figure. The upper part of panels (a) and (b) shows the Bouguer gravity along the S1 and S2 profiles, respectively. Solid line indicates the observed gravity field and the dashed line the modelled gravity. The lower part of (a) and (b) portrays the lithospheric density structures. Small green diamonds show the interface of sediments from the Exxon map (1985); blue dots show the location of gravity inverted Moho depths; Red dots show the location of the deep seismic profiles from Makris et al. (1988); and black dots show the location of receiver function results taken from El-Isa et al. (1987), Webb et al. (2004), Al-Damegh et al. (2005), and Mechie et al. (2005) along to the location of the cross-section. (For interpretation of the references to colour in this figure legend, the reader is referred to the web version of this article.)

5. Results

The gravity-based results are reported and then cross-compared with the findings of some of the previous seismic studies (Section 2.2). Such comparisons are thoroughly done along 3 longitudinal profiles.

5.1. Isostatic field

The estimated gravity-based residual isostatic anomalies are plotted in Fig. 7 b. Such a field is characterized with a minimum, maximum, mean, and STD of -58.95 , 58.06 , 17.53 , and 13.56 mGal, respectively. For the crustal structure, in case that the implemented isostasy model-related parameters are correct, the positive values of the residual field will indicate a thinner and/or a denser crust than assumed, the negative values will infer a thicker and/or a less dense crust.

Within the estimated residual isostatic anomalies (Fig. 7 b), several interesting features are detected and explained as follow:

- (i) Negative residuals are observed beneath the Nile Delta. Possible explanations could be that this area has thick sediments, of which whose effects are not fully removed from the observed BA signal.
- (ii) The existence of a positive anomaly along the coast of the Mediterranean Sea in the north-western desert, which could be related to some denser bodies located in the crystalline crust, or might be related to the subduction complex of the African lithosphere under the Eurasia.
- (iii) The high topography along the Red Sea coast is not isostatically compensated in a local scale, according to insignificant positive isostatic anomalies.
- (iv) Beneath the Uweinat area, a positive anomaly is observed, which might be linked to a thicker crust compared to the value considered within the model setup.

5.2. Modelling prerequisites

As a first step, all the available constraints are used to build up the initial Moho model, whose gravity responses have been computed without any changes to the constrained layers (sediments and Moho topography). The calculated gravity signal deviates from the observed field represented by the high residual gravity field. Therefore, the initial Moho model has poorly explained the gravity data.

A tuning process has to be conducted by carefully shifting both

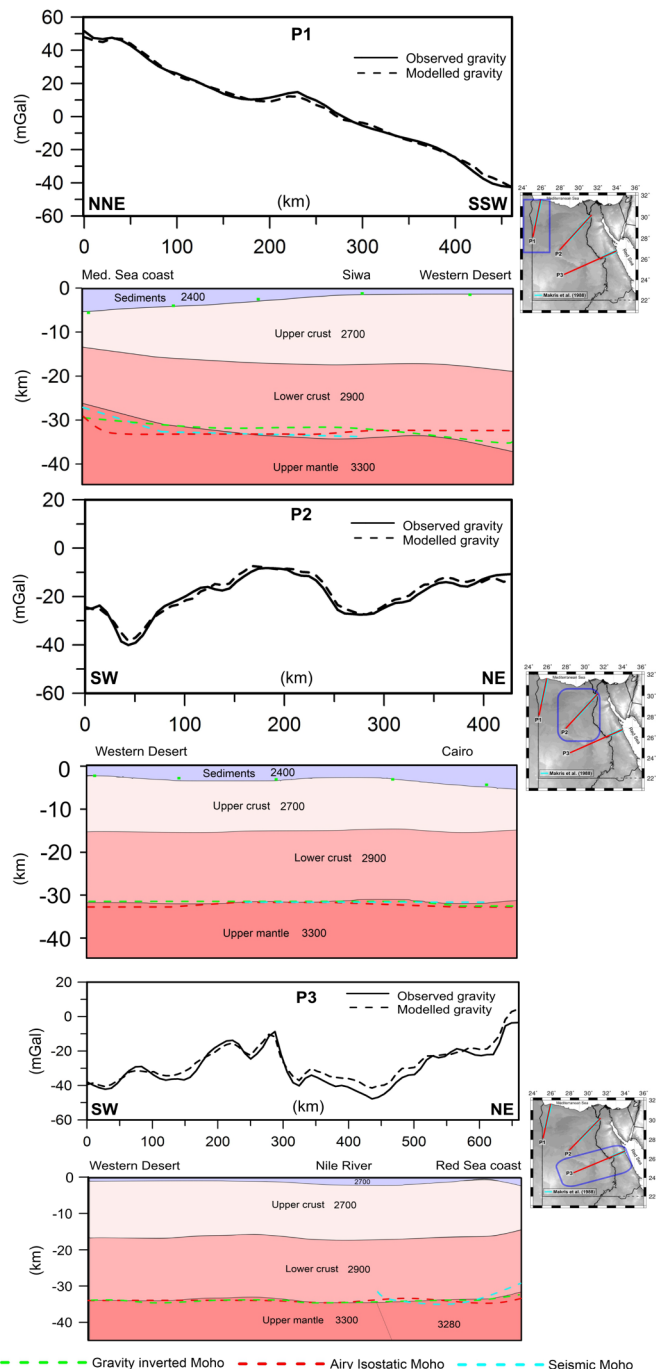


Fig. 11. Modelling results along the earlier mentioned seismic lines P1, P2, and P3, respectively. The upper panel shows the gravity field of each. Solid black lines indicate the observed gravity field, and the dashed black lines indicate the modelled gravity. In the corresponding lower panel, the density structure of the lithosphere is displayed and any black lines represent the layer boundaries. Green diamonds show the location of sediments from the Exxon map (1985); Green dashed lines show the location of gravity inverted Moho depths. See Fig. 6, red dashed line indicates the Airy isostatic Moho, cyan dashed lines show the location of the deep seismic profiles from Makris et al. (1988). (For interpretation of the references to colour in this figure legend, the reader is referred to the web version of this article.)

layers surface (the Moho depths and sedimentary thickness) to improve the fit of the gravity signal. The initial Moho model has been carefully modified at every trial except when the depths are constrained by seismic data and/or when the basement is constrained by borehole information. The density contrast, between the crystalline crust and the

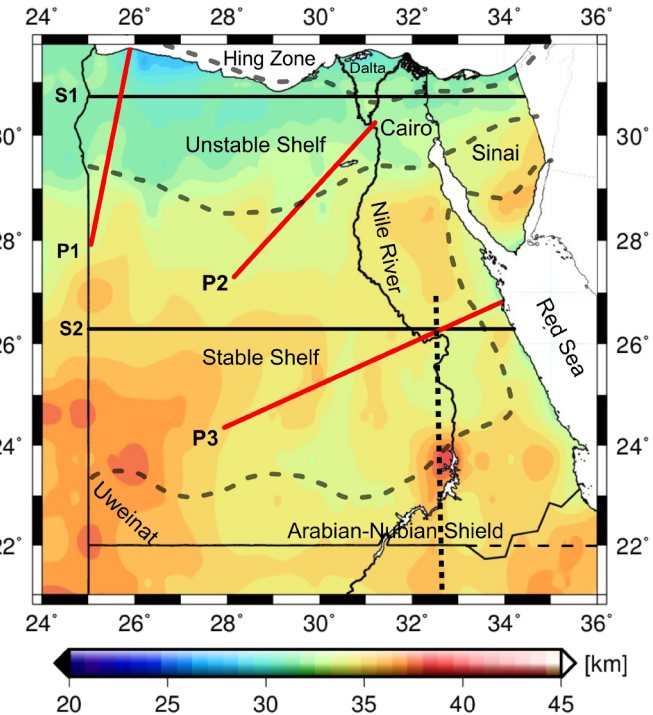


Fig. 12. The crustal thickness map determined from the 3D gravity modelling with the major geological units indicated. As before, black lines show the geographic locations of the model cross-sections S1 and S2. Dashed grey lines correspond to the main tectonic boundaries (refer also to Fig. 2), black dashed line is the Keraf shear zone between the Neoproterozoic terranes and the Saharan Metacraton drawn by Abdelsalam et al. (1998).

sediments, caused shorter wavelengths gravity anomalies than those of deeper density contrasts, for example, in the crystalline crust or the upper mantle. From the modelled BA gravity map, shown in Fig. 8 a, the main features on both maps, the measured and the modelled gravity signal, are cross-comparable with small noticeable differences in shape. The spatial distributions of the residual gravity anomalies are reported in Fig. 8 b. The average misfit between the measured and calculated anomalies reveals a correlation coefficient of 0.91 and a STD of 10 mGal, which is an acceptable value for regional gravity field modelling.

The gravity response of the modelled sediments thickness was calculated and presented in Fig. 9 a. In the southern part and along the Red Sea Mountains, the gravity response ranges between –5 and –10 mGal and it increases northward and toward the Nile Delta and the Mediterranean Sea coast. Along the Nile Delta, where the sediments thickness reaches 9 km, the gravity response decreases to –90 mGal. Since the sediment thickness map has a coarse resolution of 1 arc-degree compared to the gravity data that has a finer resolution, an uncertainty is introduced by the interpolation of the sedimentary map.

In Figs. 10 and 11, only five out of a total number of 18 vertical cross-sections, of the final model, are displayed. Two of these profiles are running in the East-West direction, where the other three profiles coincide with the seismic lines.

5.2.1. East–West profiles of the 3D density model

The profile S1, see Fig. 10, is realized along the West–East direction over a distance of about 1000 km, on which its gravity model is shown in Fig. 10 a. The undulation of the short wavelengths is due to the variations of the sediment thicknesses, whereas the western part has a sedimentary layer of 4 km thick increasing toward the Nile River, then decreases toward the eastern direction that coincides with the Red Sea Mountains. In addition, the final model confirms the presence of a steep increase in the crustal thickness toward the East close to the Red Sea

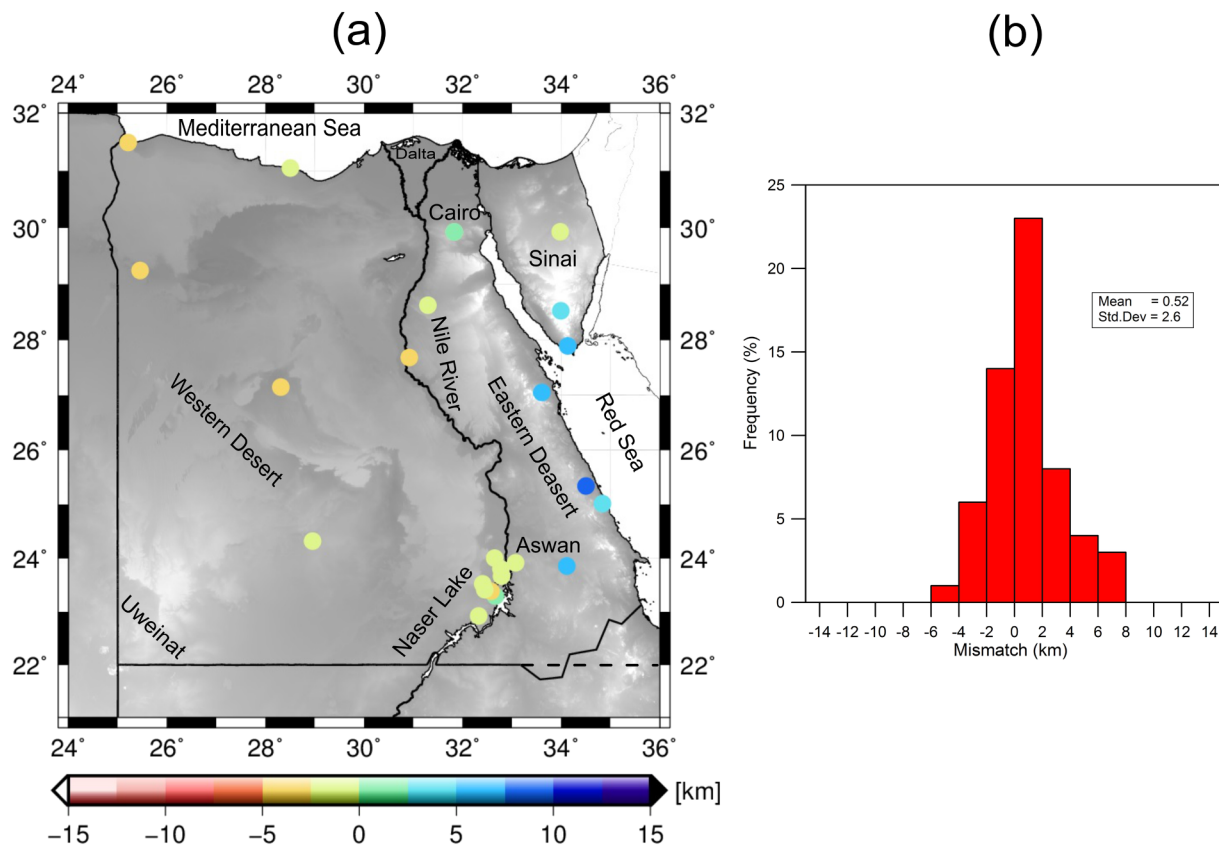


Fig. 13. A comparison between seismic based results and gravity modelling. (a) The differences between the Moho depths from receiver functions analysis and gravity-modelled Moho depths; units in [km]. (b) The histogram of the differences with their corresponding mean and standard deviation values; units in [km]. As shown in panel (b), the differences are around 0.5 km, which indicate that the gravity-derived Moho is in agreement with the depths derived from receiver functions analysis.

coastline. The estimated Moho depths range between 33 and 35 km at the West direction and gradually decrease and get steeper and/or shallower close to the Red Sea coastline, with a value of about 28–30 km.

The profile S2, demonstrated in Fig. 10 b and c, is oriented in West-East direction on the North of the study area. The western part is characterized by deep sediments along the Mediterranean Sea coastline, whose thickness increases toward the East direction reaching a maximum value of about ~ 7–8 km beneath the Nile Delta. The Moho depth is clearly shallow at the western part, which coincides with the Mediterranean Sea coastline, and then increases toward the East beneath the Nile Delta reaching values up to 32 km, and then it slightly gets shallower to the further West-side.

5.2.2. Vertical cross-sections of the 3D density modelling along seismic profiles

Three cross-sections are taken, where the seismic refraction profiles were carried out.

The profile P1 extends from the Mediterranean Sea coast to the Egyptian-Libyan border. It stretches in the NW–SE direction, see Fig. 11 a, for about 450 km through the topographic feature of the Qattara Depression. Toward the Mediterranean coast, the observed gravity values increase with the increase of the thickness of the sediments and coincide with the thin Moho thickness of about ~ 28 km with significant differences with respect to the isostatic Moho while being in a good agreement with the seismic-based Moho values.

The trending profile P2 extends from the Western Desert, oriented in a NE–SW direction, crosses the northern part of Egypt and ends at Cairo (Fig. 11 b). This profile corresponds to the seismic refraction profile of Makris et al. (1988), see the cyan dotted line in Fig. 1. The Moho depth below the Western Desert is 33 km that decreases eastward reaching a depth of 30 km beneath Cairo. The modelled Moho along this profile is in good agreement with the gravity inverted Moho (blue dotted line) but in the meanwhile is characterized with small discrepancies with respect to the isostatic Moho (red dotted line) of about ~ 2 km indicating that the area is close to its isostatic equilibrium state.

The profile P3 that extends in the NE–SW direction, runs along the seismic refraction profile of Makris et al. (1988) from the Western Desert across the Nile River and the Eastern Desert and ends at the Red Sea coastline, see Fig. 11 c. Westward, the crustal depth below the Western Desert is about ~ 33 km and gradually decreases to reach a value of ~ 31 km then increases eastward to reach its maximum value of ~ 35 km below the Red Sea hills. The Moho depths decrease toward the Red Sea coastline to a value of about ~ 28 km.

Our Moho depths estimation is in good agreements with the seismic-based Moho illustrating a small discrepancy along the Red Sea coast.

The Moho depth increases south-westward reaching a value of 31 km beneath the Siwa Oasis then gradually increases toward the southwest up to 35 km with good agreement with the gravity-inverted Moho values.

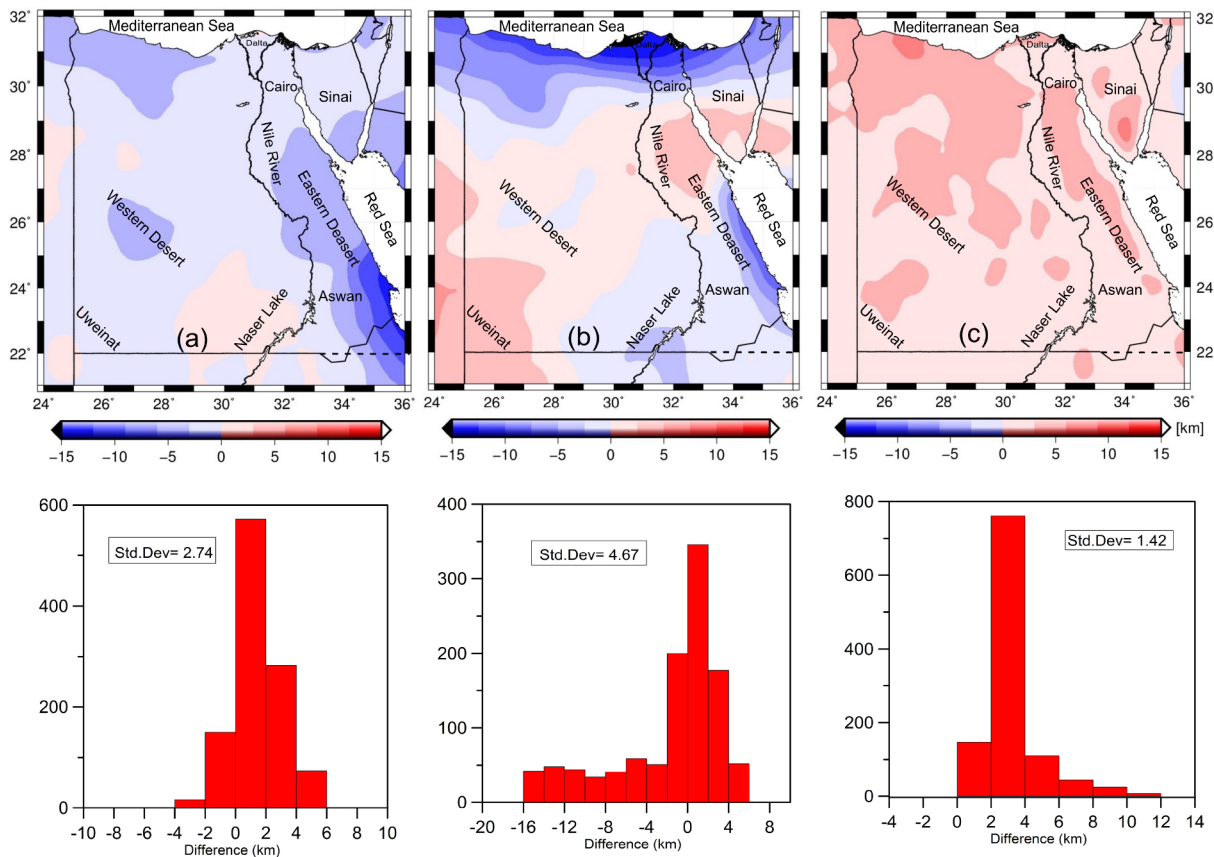


Fig. 14. Comparison between regional crustal thickness models and the model developed in the current study. Thickness differences between the “gravity based” thickness from the (a) CRUST1.0 model by Laske et al. (2013), (b) GEMMA model by Reguzzoni et al. (2013), and (c) Globig model by Globig et al. (2016). The top panels report the residuals of the three seismic “reference” models with respect to the crustal thickness calculated in this study; units in [km]. The bottom panel portrays histograms of differences between the developed model and the CRUST1.0, GEMMA, and Globig2016, respectively; units in [km].

Table 3

Statistical comparison between referenced crustal models and the new density model; units in [km].

Model	Min	Max	RMSE
CRUST1.0 — the developed model	-5.76	3.50	2.74
GEMMA — the developed model	-15.97	5.84	4.67
Globig2016 — the developed model	-0.80	11.50	1.42

6. Discussion

The obtained gravity-based Moho depths results are cross-compared with the previous seismic-based estimates, both at local and regional scales.

6.1. Moho depths estimates compared with the main geological units

The residuals of our final Moho depth estimates compared to the local and global Moho values are displayed in Fig. 12. The Moho depths map overlie the main geological units in the study area, as seen in Fig. 12, where the Moho depths spatially vary between 25 and 45 km throughout Egypt. Generally, areas with a significant Moho depth gradient correlate well with the major tectonic boundaries. The deepest Moho value was found along the Uweinat Mountains, reaching a depth value of 45 km. The pronounced Moho depth around Nasser Lake in southern Egypt is interpreted to be along the mapped Precambrian suture zone, the Keraf shear zone, which was likely formed during the collision between East Gondwana and the Sahara Metacraton during

the final assembly of Gondwana in the Neoproterozoic (Abdelsalam and Stern, 1996a; Abdelsalam and Stern, 1996b; Abdelsalam et al., 1998; Hosny and Nyblade, 2016). These tectonic units are associated with the “Arabian-Nubian Shield”. The map displayed in Fig. 12, clearly reveals both the northward and the eastward crustal thinning trends toward the Mediterranean Sea and the Red Sea, respectively. Eastward, the Moho depths beneath the Eastern Desert are situated at a depth of ~31 km. The crustal thickness varies within the Sinai Peninsula from the southern edge to the North side, which provides an evidence for the presence of an Early Mesozoic passive margin with thinned continental crust in the North of Sinai. The shallower depth of the Moho in the southern Sinai reflects a thinning phenomenon related to the rifting process in the Gulf of Suez. Linking our findings to the tectonic map of Egypt, the final Moho depths model presents a rapid thinning crust toward the Mediterranean Sea, which coincides with the Hinge Zone.

6.2. Comparison with local seismic-based Moho depths

Our estimated Moho depths are in good agreement with those obtained from seismic investigations, regardless of the available seismic data which are sparsely distributed. Fig. 13 a displays the differences between the seismic-derived Moho depths and gravity-derived model (Fig. 12). The differences approximately range between -5.0 and 7.5 km (Fig. 13 b) with a mean value of 0.52 km and a STD of 2.6 km. Along the Red Sea coastline, our model slightly overestimates the Moho depths of approximately 31 km with a difference of 5 to 7 km. On the other hand, our Moho model could produce a more reliable depths estimation, when the coverage of the seismic data is very limited, and from the literature, acceptable Moho depths discrepancies can reach

10 km (Knapmeyer-Endrun et al., 2014).

6.3. Comparison of regional Moho models

A regional comparison of our gravity-derived Moho depths model with respect to the global seismic crustal model CRUST1.0 (Laske, 1997; Laske et al., 2013), shown in Fig. 14 a, revealed significant differences. In addition, our findings were cross-compared with two gravity-derived continental-scale models, namely, the GOCE Exploitation for Moho Modelling and Applications, known as the GEMMA model (Reguzzoni et al., 2013; Reguzzoni and Sampietro, 2015), and the Globig2016 model (Globig et al., 2016). Table 3 summarizes the statistics of the differences of such comparisons.

The comparison with the GEMMA model, see Fig. 14 b, which is a gravimetric-based Moho model computed exploiting both the CRUST1.0 and GOCE data, illustrated that an overall thicker crust, with differences ranging from –5 to 5 km for most of the study area is obtained.

The Globig2016 model, displayed in Fig. 14 c, revealed the minimum root-mean-squared error (RMSE) value of 1.42 km. Although the RMSE varies between 1.7 and 4.7 km for all comparisons, the minimum and maximum crustal variations range from –15.97 to 11.5 km, indicating that in some regions, differences can be pronounced. Generally speaking, our crustal model is much thinner than the Globig2016 model, with differences ranging from 0 to 5 km for most of the study area. A note must be taken that the Globig2016 model is developed based on the joint modelling of the elevation and geoid data, combined with thermal analyses under the assumptions of local isostasy and thermal steady-state conditions.

6.4. Errors of Moho depth estimations

The accuracy of the estimated gravity-based Moho depths depends on several factors, related to the quality of the input gravity data, the applied corrections, the constraining seismic data, the availability of a precise topographic model, and the sediment thickness. With regard to the used receiver functions data for the determination of the Moho interface, an average error of about ± 4 km was indicated for Egypt (Hosny and Nyblade, 2016).

The Moho depth uncertainties attributed to the errors of the gravity data are relatively small as the accuracy of the input gravity signal and the corresponding applied corrections are of about ± 7 mGal or better. Specifically, the uncertainty of the FA anomaly provided by the Getech is ± 5 mGal (Sobh et al., 2018). The TC has an error of ~ 2 mGal, which is caused by the 6 m mean error, over North Africa, of the SRTM model (Rodriguez et al., 2006). Moreover, the TC computed with a constant density value of $2670 \text{ kg} \cdot \text{m}^{-3}$ for all rock masses above the mean sea level, would contribute an additional error during the computation of the TC and the estimation of the Moho depths.

7. Conclusions

Based on the combination of the Bott's method with Tikhonov regularization, the anomalous Moho has been discretized using the Tesseroids, in order to develop the first order Moho depths map that would be consequently used as an initial layer for the 3D forward gravity modelling performed by the (IGMAS+ software package) over Egypt. Then, such a 3D model is fed with precise topographic values.

The obtained results are cross-compared with the available seismic data and the Airy-type local isostatic compensation model. A significant correlation between the crustal thicknesses, elevation values, and Bouguer gravity advocates that the crust is approximately isostatically compensated.

The 3D gravity model was constrained using the available deep seismic profiles, receiver functions, and geological information in order to produce a regional model of the crustal thickness for the continental

part of Egypt.

The developed Moho depths model was compared with compilations of the seismic estimates showing good agreements as well as high levels of consistency.

The modelled Moho depths clearly exposed both the northward and eastward crustal thinning trends toward the Mediterranean Sea and the Red Sea, respectively. Eastward, the Moho under the Eastern Desert is located at a depth of ~ 31 km, which increases in southern Egypt to values ranging from 35 to 40 km. A maximum crustal thickness of 45 km is found in the southwestern part of Egypt. Within Sinai, the crustal thickness varies from being shallow at the southern edge to a deeper Moho toward the North. Our model revealed a thick lower crust beneath the southern part of Egypt that can be associated with the modification of the crust that occurred during the collision between East Gondwana and the Sahara Metacraton along the Kerat suture zone during the final assembly of Gondwana in the Neoproterozoic.

Our findings clearly demonstrate the advantage of gravity data inversion in studying the 3D density structure of geologically-interesting formations, where the Bouguer anomaly data is combined with a priori information retrieved from petrophysical (e.g., density values) and seismic datasets. Compared to previous studies, the developed gravity-based Moho model shows a better match with the available seismic studies than that of the global crustal model (e.g., the CRUST1.0 and GEMMA), in which the interpolation of such global models on local scales might produce unrealistic Moho depth values.

This study has mainly focused on the continental crust, where successive studies targeting the entire lithospheric scale incorporating seismic tomography and ideally petrological data are highly recommended.

Acknowledgments

The presented work has been supported by the German Academic Exchange Service (DAAD).

References

- Abdelrahman, E., Refai, E., El-Ghalban, H., 1988. Gravity models of the Nile Delta basin, Egypt. In: Egyptian Geological Survey Proceedings of 6th Annual Meeting, pp. 33.
- Abdelsalam, M., Stern, R., 1996a. Mapping Precambrian structures in the Sahara Desert with sirc/xsar radar: the Neoproterozoic Kerat suture, NE Sudan. J. Geophys. Res. Planets 101, 23063–23076. <https://agupubs.onlinelibrary.wiley.com/doi/abs/10.1029/96JE01391>, <https://doi.org/10.1029/96JE01391>.
- Abdelsalam, M., Stern, R., 1996b. Sutures and shear zones in the Arabian-Nubian Shield. J. Afr. Earth Sci. 23, 289–310. <http://www.sciencedirect.com/science/article/pii/S0899536297000031>, [https://doi.org/10.1016/S0899-5362\(97\)00003-1](https://doi.org/10.1016/S0899-5362(97)00003-1). IGCP 348 (Mozambique and Related Belts).
- Abdelsalam, M., Stern, R., Copeland, P., Elfaki, E., Elhur, B., Ibrahim, F., 1998. The Neoproterozoic Kerat suture in NE Sudan: sinistral transpression along the eastern margin of West Gondwana. J. Geol. 106, 133–148. <https://doi.org/10.1086/516012>.
- Abdelwahab, M., El-Khrepy, S., Qaddah, A., 2013. Three-dimensional structure of Conrad and Moho discontinuities in Egypt. J. Afr. Earth Sci. 85, 87–102. <http://www.sciencedirect.com/science/article/pii/S1464343X13000836>, <https://doi.org/10.1016/j.jafrearsci.2013.04.007>.
- Aitken, A., Salmon, M., Kennett, B., 2013. Australia's Moho: a test of the usefulness of gravity modelling for the determination of Moho depth. Tectonophysics 609, 468–479. <http://www.sciencedirect.com/science/article/pii/S0040195112003745>, <https://doi.org/10.1016/j.tecto.2012.06.049>. Moho: 100 years after Andrija Mohorovicic.
- Al-Damegh, K., Sandvol, E., Barazangi, M., 2005. Crustal structure of the Arabian plate: new constraints from the analysis of teleseismic receiver functions. Earth Planet. Sci. Lett. 231, 177–196. <http://www.sciencedirect.com/science/article/pii/S0012821X04007381>, <https://doi.org/10.1016/j.epsl.2004.12.020>.
- Al-Misriyah al-Ammah lil-Misraha al-Jiyulujiyah wa al Mashruaat al Taadiniyah, H., 1981. Geologic Map of Egypt.
- Allen, P., Allen, J., 2005. Basin Analysis: Principles and Applications. Wiley-Blackwell.
- Alvers, M., Barrio-Alvers, L., Bodor, C., Götz, H.-J., Lahrneyer, B., Plonka, C., Schmidt, S., 2015. ? quo vadis inversión? First Break 33, 65–74.
- Alvers, M., Götz, H.-J., Barrio-Alvers, L., Schmidt, S., Lahmeyer, B., Plonka, C., 2014. A novel warped-space concept for interactive 3d-geometry-inversion to improve seismic imaging. First Break 32.
- Amante, C., 2009. Etopo1 1 arc-minute global relief model: procedures, data sources and analysis. <http://www.ngdc.noaa.gov/mgg/global/global.html>.
- Baschlin, C., 1948. Lehrbuch der geodäsie. Verlag Orell Füssli, Zurich.

- Bouman, J., Ebbing, J., Meekes, S., Fattah, R.A., Fuchs, M., Gradmann, S., Haagmans, R., Lieb, V., Schmidt, M., Dettmering, D., Bosch, W., 2015. GOCE gravity gradient data for lithospheric modeling. *Int. J. Appl. Earth Obs. Geoinf.* 35, 16–30. <http://www.sciencedirect.com/science/article/pii/S0303243413001487>, <https://doi.org/10.1016/j.jag.2013.11.001>. GOCE earth science applications and models (Based on the ESA GOCE Solid Earth Workshop, 16–17 October 2012).
- Braatenberg, C., Sampietro, D., Pivetta, T., Zuliani, D., Barbagallo, A., Fabris, P., Rossi, L., Fabbri, J., Mansi, A.H., 2016, Apr, Apr. Gravity for detecting caves: airborne and terrestrial simulations based on a comprehensive karstic cave benchmark. *Pure Appl. Geophys.* 173, 1243–1264. <https://doi.org/10.1007/s00024-015-1182-y>.
- Capponi, M., Mansi, A., Sampietro, D., 2018, Apr, Apr. Improving the computation of the gravitational terrain effect close to ground stations in the GTE software. *Stud. Geophys. Geod.* 62, 206–222. <https://doi.org/10.1007/s11200-017-0814-3>.
- Christensen, N., Mooney, W., 1995. Seismic velocity structure and composition of the continental crust: a global view. *J. Geophys. Res. Solid Earth* 100, 9761–9788. <https://agupubs.onlinelibrary.wiley.com/doi/abs/10.1029/95JB00259>, <https://doi.org/10.1029/95JB00259>.
- Cochetche, V., Chourak, M., Hussein, H., Atiya, K., Timoulali, Y., 2017. Crustal and upper mantle structure of the north-east of Egypt and the Afro-Arabian plate boundary region from Rayleigh-wave analysis. *J. Afr. Earth Sci.* 129, 195–201. <http://www.sciencedirect.com/science/article/pii/S1464343X17300122>, <https://doi.org/10.1016/j.jafrearsci.2017.01.011>.
- Dorre, A., Carrara, E., Celli, F., Grimaldi, M., Hady, Y., Hassan, H., Rapolla, A., Roberti, N., 1997. Crustal thickness of Egypt determined by gravity data. *J. Afr. Earth Sci.* 25, 425–434. <http://www.sciencedirect.com/science/article/pii/S0899536297001140>, [https://doi.org/10.1016/S0899-5362\(97\)00114-0](https://doi.org/10.1016/S0899-5362(97)00114-0).
- EL-Hadidy, S., 1995. Crustal Structure and its Related Causative Tectonics in Northern Egypt Using Geophysical Data, Egypt. Ph.D. thesis. Ain Shams University.
- El-Isa, Z., Mechie, J., Prodehl, C., Makris, J., Rihm, R., 1987. A crustal structure study of Jordan derived from seismic refraction data. *Tectonophysics* 138, 235–253. <http://www.sciencedirect.com/science/article/pii/0040195187900424>, [https://doi.org/10.1016/0040-1951\(87\)90042-4](https://doi.org/10.1016/0040-1951(87)90042-4).
- El-Khrepy, S., 2001. Tomographic Modeling of Dahshour Area Local Earthquakes, Northern Egypt. M.Sc. thesis. Ain Shams University.
- El-Khrepy, S., 2008. Detailed Study of the Seismic Waves Velocity and Attenuation Models Using Local Earthquakes in the Northeastern Part of Egypt, Mansoura, Egypt. Ph.D. thesis. Mansoura University.
- Exxon, 1985. Tectonic Map Series of the World. Exxon Production Research Company, Houston, TX, USA.
- Fairhead, J., Watts, A., Chevalier, P., El-Haddadeh, B., Green, C., Stuart, G., Whaler, K., Whindle, I., 1988. African Gravity Project. GETECH, Department of Earth Sciences, University of Leeds.
- Gaulier, J., Pichon, X., Lyberis, N., Avedik, F., Geli, L., Moretti, I., Deschamps, A., Hafez, S., 1988. Seismic study of the crust of the northern Red Sea and Gulf of Suez. *Tectonophysics* 153, 55–88. <http://www.sciencedirect.com/science/article/pii/0040195188900078>, [https://doi.org/10.1016/0040-1951\(88\)90007-8](https://doi.org/10.1016/0040-1951(88)90007-8). The Gulf of Suez and Red Sea rifting.
- Ginzburg, A., Ben-Avraham, Z., 1987. The deep structure of the central and southern Levant continental margin. In: *Annales Tectonicae*, pp. 105–115.
- Ginzburg, A., Makris, J., Fuchs, K., Prodehl, C., 1981. The structure of the crust and upper mantle in the Dead Sea Rift. *Tectonophysics* 80, 109–119. <http://www.sciencedirect.com/science/article/pii/004019518190144X>, [https://doi.org/10.1016/0040-1951\(81\)90144-X](https://doi.org/10.1016/0040-1951(81)90144-X). The Dead Sea Rift.
- Globig, J., Fernández, M., Torne, M., Vergés, J., Robert, A., Faccenna, C., 2016. New insights into the crust and lithospheric mantle structure of Africa from elevation, geoid, and thermal analysis. *J. Geophys. Res. Solid Earth* 121, 5389–5424. <https://agupubs.onlinelibrary.wiley.com/doi/abs/10.1002/2016JB012972>, <https://doi.org/10.1002/2016JB012972>.
- Götze, H., Lahmeyer, B., 1988. Application of three-dimensional interactive modeling in gravity and magnetics. *Geophysics* 53, 1096–1108. <https://doi.org/10.1190/1.1442546>.
- Hackney, R., Featherstone, W., 2003. Geodetic versus geophysical perspectives of the ‘gravity anomaly’. *Geophys. J. Int.* 154, 35–43. <https://doi.org/10.1046/j.1365-246X.2003.01941.x>.
- Hantschel, T., Kauerauf, A., 2009. *Fundamentals of Basin and Petroleum Systems Modeling*. Springer Science & Business Media.
- Hinze, W., Aiken, C., Brozena, J., Coakley, B., Dater, D., Flanagan, G., Forsberg, R., Hildenbrand, T., Keller, G., Kellogg, J., Kucks, R., Li, X., Mainville, A., Morin, R., Pilkington, M., Plouff, D., Ravat, D., Roman, D., Urrutia-Fucugauchi, J., Véronneau, M., Webring, M., Winester, D., 2005. New standards for reducing gravity data: the North American gravity database. *Geophysics* 70, J25–J32. <https://doi.org/10.1190/1.1988183>.
- Hosny, A., Nyblade, A., 2014. Crustal structure in southeastern Egypt: symmetric thinning of the northern Red Sea rifted margins. *Geology* 42, 219. <https://doi.org/10.1130/G34726.1>.
- Hosny, A., Nyblade, A., 2016. The crustal structure of Egypt and the northern Red Sea region. *Tectonophysics* 687, 257–267. <http://www.sciencedirect.com/science/article/pii/S0040195116302104>, <https://doi.org/10.1016/j.tecto.2016.06.003>.
- Jacobs, J., Russell, R., Wilson, J., 1959. *Physics and Geology*. McGraw-Hill Book Co., New York.
- Kaban, M., Stolk, W., Tesauro, M., El Khrepy, S., AlââR Arifi, N., Beekman, F., Cloetingh, S., 2016. 3D density model of the upper mantle of Asia based on inversion of gravity and seismic tomography data. *Geochem. Geophys. Geosyst.* 17, 4457–4477. <https://agupubs.onlinelibrary.wiley.com/doi/abs/10.1002/2016GC006458>, <https://doi.org/10.1002/2016GC006458>.
- Knapmeyer-Endrun, B., Krüger, F., Group, T., 2014. Moho depth across the trans-European suture zone from p- and s-receiver functions. *Geophys. J. Int.* 197 (2), 1048–1075. <https://doi.org/10.1093/gji/ggu035>.
- LaFehr, T., 1991. An exact solution for the gravity curvature (Bullard b) correction. *Geophysics* 56, 1179–1184. <https://doi.org/10.1190/1.1443138>.
- Laske, G., 1997. A global digital map of sediment thickness. *EOS Trans. Am. Geophys. Union* 78, F483.
- Laske, G., Masters, G., Ma, Z., Pasquano, M., 2013. Update on crust1.0—a 1-degree global model of earth's crust. In: *Geophys Res Abstr.*, pp. 2658.
- Li, X., Götz, H., 2001. Ellipsoid, geoid, gravity, geodesy, and geophysics. *Geophysics* 66, 1660–1668. <https://doi.org/10.1190/1.1487109>.
- Makris, J., 1983. Crustal structure at the northwestern region of the Arabian Shield and its transition to the Red Sea. In: *Bulletin of the Faculty of Earth Sciences*. 6. King Abdulaziz University, pp. 435–447.
- Makris, J., Henke, C., Egloff, F., Akamaluk, T., 1991. The gravity field of the Red Sea and East Africa. *Tectonophysics* 198, 369–381. <http://www.sciencedirect.com/science/article/pii/0040195190161K>, [https://doi.org/10.1016/0040-1951\(91\)90161-K](https://doi.org/10.1016/0040-1951(91)90161-K). Red Sea Birth and Early History of a New Oceanic Basin.
- Makris, J., Rihm, R., 1991. Shear-controlled evolution of the Red Sea: pull apart model. *Tectonophysics* 198, 441–466. <http://www.sciencedirect.com/science/article/pii/0040195190166P>, [https://doi.org/10.1016/0040-1951\(91\)90166-P](https://doi.org/10.1016/0040-1951(91)90166-P). Red Sea: Birth and Early History of a New Oceanic Basin.
- Makris, J., Rihm, R., Allam, A., Maamoun, M., Shehata, W., 1979. Deep seismic sounding in Egypt, part i: the Mediterranean Sea between Crete, Sidi Barani, and the coastal area of Egypt. Unpublished report, National Research Institute of Astronomy and Geophysics, Helwan, Egypt.
- Makris, J., Wang, J., Odintsov, S., Udintsev, G., 1994. Geological Structure of the Northeastern Mediterranean: (Cruise 5 of the Research Vessel Akademik Nikolaj Strakhov). *Geologicheskii Institut Akademii Nauk SSSR*.
- Mansi, A., 2016. Airborne Gravity Field Modelling. Ph.D. thesis. Politecnico di Milano. <https://www.politesi.polimi.it/handle/10589/116547>.
- Mansi, A.H., Capponi, M., Sampietro, D., 2018, Mar, Mar. Downward continuation of airborne gravity data by means of the change of boundary approach. *Pure Appl. Geophys.* 175, 977–988. <https://doi.org/10.1007/s00024-017-1717-5>.
- Marzouk, I., 1988. Crustal Structure of Egypt Deduced From Deep Seismic and Gravity Data. Ph.D. dissertation. 118 Univ. of Hamburg.
- Mayer-Guerr, T., 2015. The combined satellite gravity field model GOCO05s.
- Mechie, J., Abu-Ayyash, K., Ben-Avraham, Z., El-Kelani, R., Mohsen, A., Rümpker, G., Saul, J., Weber, M., 2005. Crustal shear velocity structure across the Dead Sea transform from two-dimensional modelling of desert project explosion seismic data. *Geophys. J. Int.* 160, 910–924. <https://doi.org/10.1111/j.1365-246X.2005.02526.x>.
- Mikuška, J., Paštěka, R., Marušiak, I., 2006. Estimation of distant relief effect in gravimetry. *Geophysics* 71, J59–J69. <https://doi.org/10.1190/1.2338333>.
- Naudy, H., Neumann, R., 1965. Sur la définition de l'anomalie de bouguer et ses conséquences pratiques. *Geophys. Prospect.* 13, 1–11.
- Ngalamo, J.F.G., Sobh, M., Bisso, D., Abdelsalam, M.G., Atekwa, E., Ekodeck, G.E., 2018. Lithospheric structure beneath the Central Africa Orogenic Belt in Cameroon from the analysis of satellite gravity and passive seismic data. *Tectonophysics* 745, 326–337. <http://www.sciencedirect.com/science/article/pii/S0040195118302932>, <https://doi.org/10.1016/j.tecto.2018.08.015>.
- Prodehl, C., Mechic, J., 1991. Crustal thinning in relationship to the evolution of the Afro-Arabian rift system: a review of seismic-refraction data. *Tectonophysics* 198, 311–327. <http://www.sciencedirect.com/science/article/pii/00401951901580>, [https://doi.org/10.1016/0040-1951\(91\)90158-O](https://doi.org/10.1016/0040-1951(91)90158-O). Red Sea: Birth and Early History of a New Oceanic Basin.
- Rabbel, W., Kaban, M., Tesauro, M., 2013. Contrasts of seismic velocity, density and strength across the Moho. *Tectonophysics* 609, 437–455. <http://www.sciencedirect.com/science/article/pii/S0040195113003855>, <https://doi.org/10.1016/j.tecto.2013.06.020>. Moho: 100 years after Andrija Mohorovičić.
- Reguzzoni, M., Sampietro, D., 2015. Gemma: an earth crustal model based on GOCE satellite data. *Int. J. Appl. Earth Obs. Geoinf.* 35, 31–43. <http://www.sciencedirect.com/science/article/pii/S03032434141000865>, <https://doi.org/10.1016/j.jag.2014.04.002>. GOCE earth science applications and models (Based on the ESA GOCE Solid Earth Workshop, 16–17 October 2012).
- Reguzzoni, M., Sampietro, D., Sansò, F., 2013. Global Moho from the combination of the CRUST2.0 model and GOCE data. *Geophys. J. Int.* 195, 222–237. <https://doi.org/10.1093/gji/ggt247>.
- Rihm, R., 1984. Seismische Messungen im Roten Meer und ihre Interpretation. Ph.D. thesis. Inst. für Geophysik Univ. Hamburg.
- Rihm, R., Makris, J., Möller, L., 1991. Seismic surveys in the northern Red Sea: asymmetric crustal structure. *Tectonophysics* 198, 279–295. <http://www.sciencedirect.com/science/article/pii/0040195190156M>, [https://doi.org/10.1016/0040-1951\(90156-M](https://doi.org/10.1016/0040-1951(90156-M)). Red Sea: Birth and Early History of a New Oceanic Basin.
- Rodriguez, E., Morris, C., Belz, J., 2006. A global assessment of the SRTM performance. *Photogramm. Eng. Remote. Sens.* 72, 249–260.
- Said, R., 1962. *The Geology of Egypt*. Eivier, Amsterdam-New York.
- Salah, M., 2011. Crustal structure beneath Kottamiya broadband station, northern Egypt, from analysis of teleseismic receiver functions. *J. Afr. Earth Sci.* 60, 353–362. <http://www.sciencedirect.com/science/article/pii/S1464343X11000902>, <https://doi.org/10.1016/j.jafrearsci.2011.04.002>.
- Saleh, S., 2012. 3D crustal structure and its tectonic implication for Nile Delta and Greater Cairo regions, Egypt, from geophysical data. *Acta Geodaet. Geophys. Montanist. Hung.* 47, 402–429. <https://doi.org/10.1556/AGeod.47.2012.4.3>.

- Saleh, S., Jahr, T., Jentzsch, G., Saleh, A., Ashour, N.A., 2006. Crustal evaluation of the northern Red Sea rift and Gulf of Suez, Egypt from geophysical data: 3-dimensional modeling. *J. Afr. Earth Sci.* 45, 257–278. <http://www.sciencedirect.com/science/article/pii/S1464343X06000343>, <https://doi.org/10.1016/j.jafrearsci.2006.02.001>.
- Sampietro, D., Capponi, M., Mansi, A., Gatti, A., Marchetti, P., Sansò, F., 2017, May, May. Space-wise approach for airborne gravity data modelling. *J. Geodesy*. 91, 535–545. <https://doi.org/10.1007/s00190-016-0981-y>.
- Sampietro, D., Capponi, M., Triglione, D., Mansi, A., Marchetti, P., Sansò, F., 2016. GTE: a new software for gravitational terrain effect computation: theory and performances. *Pure Appl. Geophys.* 173, 2435–2453. <https://doi.org/10.1007/s00024-016-1265-4>.
- Sampietro, D., Mansi, A., Capponi, M., 2018a. Moho depth and crustal architecture beneath the levant basin from global gravity field model. *Geosciences* 8, 200–214. <http://www.mdpi.com/2076-3263/8/6/200>, <https://doi.org/10.3390/geosciences8060200>.
- Sampietro, D., Mansi, A., Capponi, M., 2018b. A new tool for airborne gravimetry survey simulation. *Geosciences* 8, 292–301. <http://www.mdpi.com/2076-3263/8/8/292>, <https://doi.org/10.3390/geosciences8080292>.
- Schaeffer, A., Lebedev, S., 2013. Global shear speed structure of the upper mantle and transition zone. *Geophys. J. Int.* 194, 417–449. <https://doi.org/10.1093/gji/ggt095>.
- Schmidt, S., Barrio-Alvers, L., Götze, H.-J., 2015. IGMAS+: Interactive Geophysical Modelling Assistant. Software tutorial.
- Schmidt, S., Götze, H.-J., Fichler, C., Alvers, M., 2010. IGMAS+: a new 3d gravity, FTG and magnetic modeling software. In: Zipf, A., Behncke, K., Hillen, F., Scheffermeyer, J. (Eds.), *GEO-INFORMATIK Die Welt im Netz*. Akademische Verlagsgesellschaft AKA GmbH, Heidelberg, Germany, pp. 57–63.
- Seber, D., Steer, D., Sandvol, E., Sandvol, C., Brindisi, C., Barazangi, M., 2000. Design and development of information systems for the geosciences: an application to the Middle East. *Geoarabia* 5, 269–296.
- Segev, A., Rybakov, M., Lyakhovsky, V., Hofstetter, A., Tibor, G., Goldshmidt, V., Avraham, Z.B., 2006. The structure, isostasy and gravity field of the Levant continental margin and the southeast Mediterranean area. *Tectonophysics* 425, 137–157.
- <http://www.sciencedirect.com/science/article/pii/S0040195106003611>, <https://doi.org/10.1016/j.tecto.2006.07.010>.
- Silva, J., Santos, D., Gomes, K., 2014. Fast gravity inversion of basement relief. *Geophysics* 79, G79–G91. <https://doi.org/10.1190/geo2014-0024.1>.
- Sobh, M., Mansi, A., Ebbing, J., Campbell, S., 2018. Regional gravity field model of Egypt based on the satellite and ground-based data. *Pure Appl. Geophys.* 2018, 1–20. <https://link.springer.com/article/10.1007%2Fs00024-018-1982-y>, <https://doi.org/10.1007/s00024-018-1982-y>.
- Szwilus, W., Ebbing, J., Holzrichter, N., 2016. Importance of far-field topographic and isostatic corrections for regional density modelling. *Geophys. J. Int.* 207, 274–287. <https://doi.org/10.1093/gji/ggw270>.
- Tealeb, A., Gharib, A., Hussein, A., 2003. Crustal and upper mantle structure beneath Al-Fayum short-period station from spectral analysis of p-wave amplitude ratios. *NRIAG-JAG* 2, 27–49.
- Uieda, L., Barbosa, V., 2017. Fast nonlinear gravity inversion in spherical coordinates with application to the South American Moho. *Geophys. J. Int.* 208, 162–176. <https://doi.org/10.1093/gji/ggw390>.
- Uieda, L., Barbosa, V., Braatenberg, C., 2016. Tesseroids: Forward-modeling gravitational fields in spherical coordinates. *Geophysics* 81 (5), F41–F48. <https://doi.org/10.1190/geo2015-0204.1>.
- Webb, S., Cawthorn, R., Nguuri, T., James, D., 2004. Gravity modeling of bushveld complex connectivity supported by Southern African seismic experiment results. *S. Afr. J. Geol.* 107, 207. <https://doi.org/10.2113/107.1-2.207>.
- Zaki, A., Mansi, A.H., Rabah, M., El-Fiky, G., 2018a. Validation of recently released GOCE-based satellite-only global geopotential models over the Red Sea using shipborne gravity data. *Boll. Geofis. Teor. Appl.* 59, 267–284. http://www3.ogs.trieste.it/bgta/pdf/bgta0242_Zaki.pdf, <https://doi.org/10.4430/bgta0242>.
- Zaki, A., Mansi, A.H., Selim, M., Rabah, M., El-Fiky, G., 2018b. Comparison of satellite altimetric gravity and global geopotential models with shipborne gravity in the Red Sea. *Mar. Geod.* 41, 258–269. <https://doi.org/10.1080/01490419.2017.1414088>.